1

Morphology control, self-assembly and site-selective deposition of metal oxide nanocrystals

Yoshitake Masuda
National Institute of Advanced Industrial Science and Technology (AIST), 2266-98 Anagahora, Shimoshidami, Moriyama-ku, Nagoya 463-8560, Japan

Keywords

Nanocrystals, Metal Oxide, Morphology Control, Self-assembly, Site-selective Deposition, Self-assembled Monolayer, Liquid Phase Process, Aqueous Phase Process, Aqueous Solution Process

1. Introduction

Nanocrystals of metal oxides have been attracted much attention for future science and technology. Morphology control, self-assembly and site-selective deposition of nanocrystals will open a new frontier in materials science. They were realized in this chapter using aqueous solution processes for metal oxide nanocrystals.

Site-selective deposition (SSD) of metal oxide thin films was developed to fabricate nano/microstructures of metal oxide such as TiO_2, Fe_3O_4, ZnO, Y_2O_3:Eu, etc.. Several conceptual processes for SSD using self-assembled monolayers (SAMs) as templates were proposed, and nano/micropatterns of ceramic thin films were successfully fabricated. Molecular recognition of SAMs was effectively used to achieve high site-selectivity. These processes can be used for the fabrication of various metal oxide devices under environment-friendly conditions.

We also developed a self-assembly process of particles to fabricate desired patterns of colloidal crystals. A micropattern of colloidal methanol prepared on a SAM in hexane was used as a mold for particle patterning, and slow dissolution of methanol into hexane caused shrinkage of molds to form micropatterns of close-packed particle assemblies. This result is a step toward the realization of nano/micro periodic structures for next-generation photonic devices by a self-assembly process.

Furthermore, metal oxides were synthesized in aqueous solutions to form anisotropic nanostructures. Stand-alone ZnO self-assembled films were, for instance, prepared using air-liquid interfaces. The ZnO films had sufficiently high strength to free-stand-alone and showed high *c*-axis orientation. The films can be pasted onto desired substrates. ZnO particles having a hexagonal cylinder shape, long ellipse shape or hexagonal symmetry radial whiskers were also prepared in aqueous solutions. The morphology was controlled by changing the supersaturation degree. Anatase TiO_2 particles with high surface area of 270 m^2/g were prepared at 50°C. The particles were assemblies of nano TiO_2 crystals covered with nanorelief surface structures. The crystals grew anisotropically along the *c*-axis to form

acicular crystals. TiO_2 films consisted of anisotropic acicular crystals were also prepared. The films showed high *c*-axis orientation. Acicular $BaTiO_3$ particles were prepared using morphology control of $BaC_2O_4 \bullet 0.5H_2O$. They were prepared in aqueous solutions and annealed with co-precipitated amorphous phase to form acicular $BaTiO_3$ particles.
In this chapter, we will mainly focus on "liquid phase morphology control of metal oxides nanocrystals" of ZnO[1], TiO_2[2] and $BaTiO_3$ particles[3], and "liquid phase site-selective deposition of metal oxide nanocrystals" of TiO_2[4] and Eu:Y_2O_3[5].

2. Liquid Phase Morphology Control of Metal Oxide Nanocrystals

2.1. Morphology Control of Stand-alone ZnO Self-assembled Film[1]

Stand-alone ZnO films were fabricated using aqueous solutions. The films were assemblies of sheet shaped nanocrystals. They had gradient structure, high *c*-axis orientation, high surface area and unique morphology. They were formed at the top of solutions without substrate. Air-liquid interface was used as a template in this process.
Zinc nitrate hexahydrate ($Zn(NO_3)_2$ $6H_2O$) (15 mM) was dissolved in distilled water at 60°C. Ethylenediamine ($H_2NCH_2CH_2NH_2$) (15 mM) was added to the solution to induce the formation of ZnO[1]. The solution was kept at 60°C using a water bath for 6 h with no stirring. The solution was then left to cool for 42 h in the bath. Polyethylene terephthalate (PET) film, glass (S-1225, Matsunami Glass Ind., Ltd.) and an Si wafer (p-type Si [100], NK Platz Co., Ltd.) were used as substrates.
The solution color was changed from transparent to white after the addition of ethylenediamine. ZnO particles were formed by the homogeneous nucleation and growth. The solution became transparent again after 6h. The supersaturation degree of the solution was high at the initial stage of the reaction for the first 1 h and decreased as the color of the solution changed. Ethylenediamine accelerated deposition of ZnO. Zinc-ethylenediamine complex forms in the solution as shown by eq. 1[6].

$$Zn^{2+} + 3H_2NCH_2CH_2NH_2 \rightleftharpoons [Zn(H_2NCH_2CH_2NH_2)_3]^{2+} \quad (1)$$

The chemical equilibrium in eq. 1 moves to the left and the zinc-ethylenediamine complex decomposes to increase the concentration of Zn^{2+} at elevated temperature.
OH^- concentration increases by the hydrolysis of ethylenediamine as shown by eq. 2.

$$H_2NCH_2CH_2NH_2 + 2H_2O \rightleftharpoons H_3NCH_2CH_2NH_3^{2+} + 2OH^- \quad (2)$$

ZnO and $Zn(OH)_2$ are thus formed in the aqueous solution as shown by eq. 3.

$$Zn^{2+} + 2OH^- \longrightarrow Zn(OH)_2 \longrightarrow ZnO + H_2O \quad (3)$$

Films were formed at the top of the solution. Air-liquid interface was used as template. The films had sufficiently high strength to be obtained as stand-alone films. Additionally, a film was scooped to past onto a desired substrate such PET film, Si wafer, glass plate or paper, and the pasted ZnO film was then dried to bond it to the substrate. Both sides of the film can be pasted on substrate. The film physically adhered to the substrate. The film maintained its adhesion during immersion in lightly ultrasonicated water, however, it can be easily peeled off again by strong ultrasonication. The film can be handled easily from substrate to other substrate. It also

can be attached strongly to substrate by annealing or addition of chemical regents such as silane coupling agent to form chemical bonds between the film and the substrate.

The film grew to a thickness of about 5 μm after 48 h, i.e., 60°C for 6 h, and was left to cool for 42 h.

The air side of the stand-alone film had a smooth surface over a wide area due to the flat air-liquid interface (Fig. 1-a1), whereas the liquid side of the film had a rough surface (Fig. 1-b1). The films consisted of ZnO nano-sheets were clearly observed from the liquid side (Fig. 1-b2) and the fracture edge-on profile of the film (Fig. 1-c1, 1-c2). The nano-sheets had a thickness of 5-10 nm and were 1-5 μm in size. They mainly grew forward to the bottom of the solution, i.e., perpendicular to the air-liquid interface, such that the sheets stood perpendicular to the air-liquid interface. Thus, the liquid side of the film had many ultra-fine spaces surrounded by nano-sheet and had a high specific surface area. The air side of the film, on the other hand, had a flat surface that followed the flat shape of the air-liquid interface. The air-liquid interface was thus effectively utilized to form the flat surface of the film. This flatness would contribute to the strong adhesion strength to substrates for pasting of the film. The air-side surface prepared for 48 h had holes of 100-500 nm in diameter (Fig. 1-a2), and were hexagonal, rounded hexagonal or round in shape. The air-side surface prepared for 6 h, in contrast, had no holes on the surface. The air-side surface was well crystallized to form a dense surface and ZnO crystals would partially grow to a hexagonal shape because of the hexagonal crystal structure. Well-crystallized ZnO hexagons were then etched to form holes on the surface by decrease in pH. The growth face of the film would be liquid side. ZnO nano-sheets would grow to form a large ZnO film by Zn ion supply from the aqueous solution. Further investigation of the formation mechanism would contribute to the development of crystallography in the solution system and the creation of novel ZnO fine structures.

The film showed a very strong 0002 x-ray diffraction peak of hexagonal ZnO at $2\theta = 34.04°$ and weak 0004 diffraction peak at $2\theta = 72.16°$ with no other diffractions of ZnO (Fig. 2). (0002) planes and (0004) planes were perpendicular to the *c*-axis, and the diffraction peak only from (0002) and (0004) planes indicates high *c*-axis orientation of ZnO film. The inset figure shows that the crystal structure of hexagonal ZnO stands on a substrate to make the *c*-axis perpendicular to the substrate. Crystallite size parallel to (0002) planes was estimated from the half-maximum full-width of the 0002 peak to 43 nm. This is similar to the threshold limit value of our XRD equipment and thus the crystallite size parallel to (0002) planes is estimated to be greater than or equal to 43 nm. Diffraction peaks from a silicon substrate were observed at $2\theta = 68.9°$ and $2\theta = 32.43°$. Weak diffractions at $2\theta = 12.5°$, 24.0°, 27.6°, 30.5°, 32.4° and 57.6° were assigned to co-precipitated zinc carbonate hydroxide ($Zn_5(CO_3)_2(OH)_6$, JCPDS No. 19-1458).

Stand-alone ZnO film was further evaluated by TEM and electron diffraction. The film was crushed to sheets and dispersed in an acetone. The sheets at the air-liquid interface were skimmed by a cupper grid with a carbon supporting film. The sheets were shown to have uniform thickness (Fig. 2a). They were dense polycrystalline films constructed of ZnO nanoparticles (Fig. 2b). Lattice image was clearly observed to show high crystallinity of the particles. The film was shown to be single phase of ZnO by electron diffraction pattern. These observations were consistent with XRD and SEM evaluations.

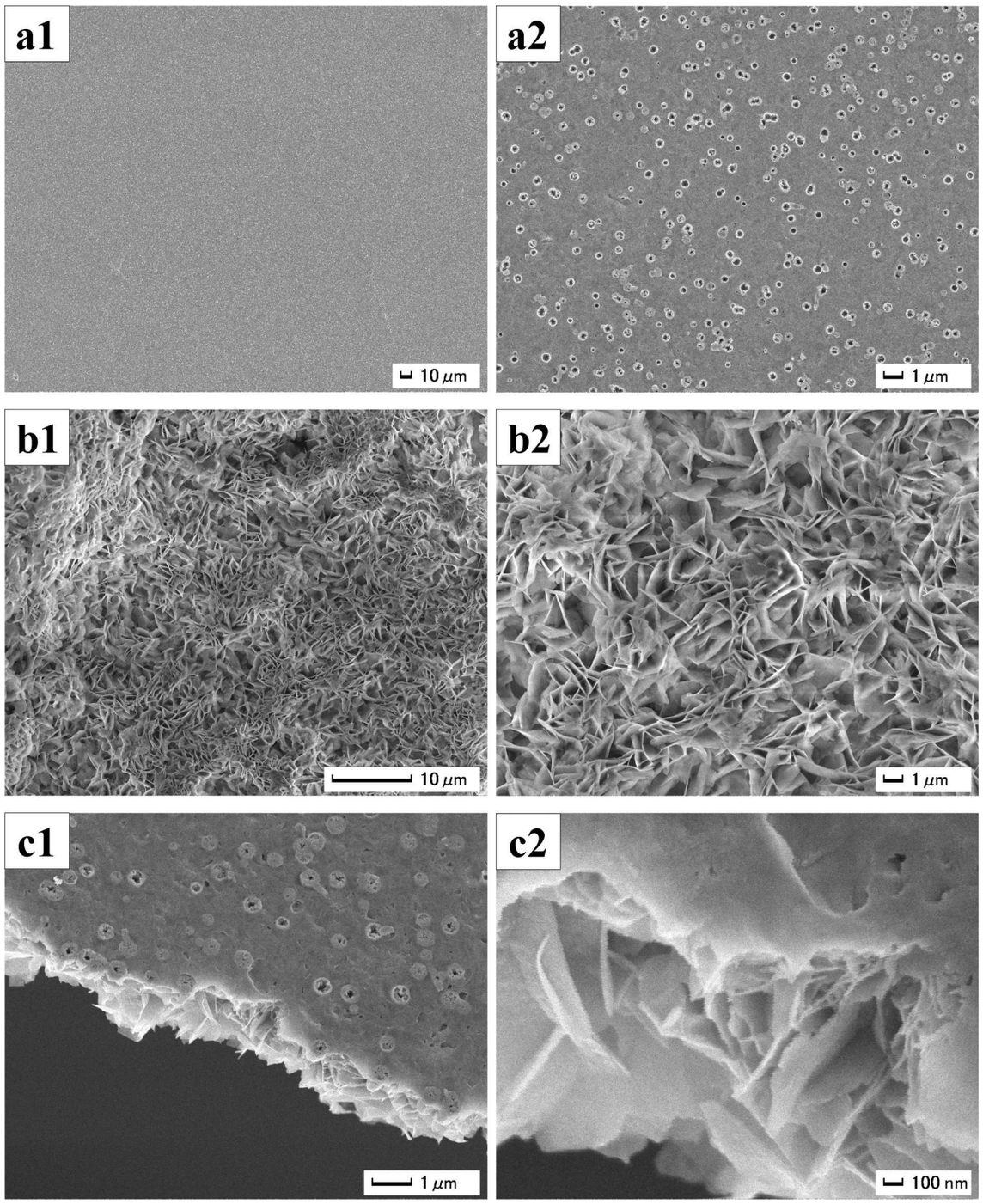

Fig. 1. SEM micrographs of high *c*-axis oriented stand-alone ZnO self-assembled film. (a1) Air-side surface of ZnO film. (a2) Magnified area of (a1). (b1) Liquid-side surface of ZnO film. (b2) Magnified area of (b2). (c1) Fracture cross section of ZnO film from air side. (c2) Magnified area of (c1).

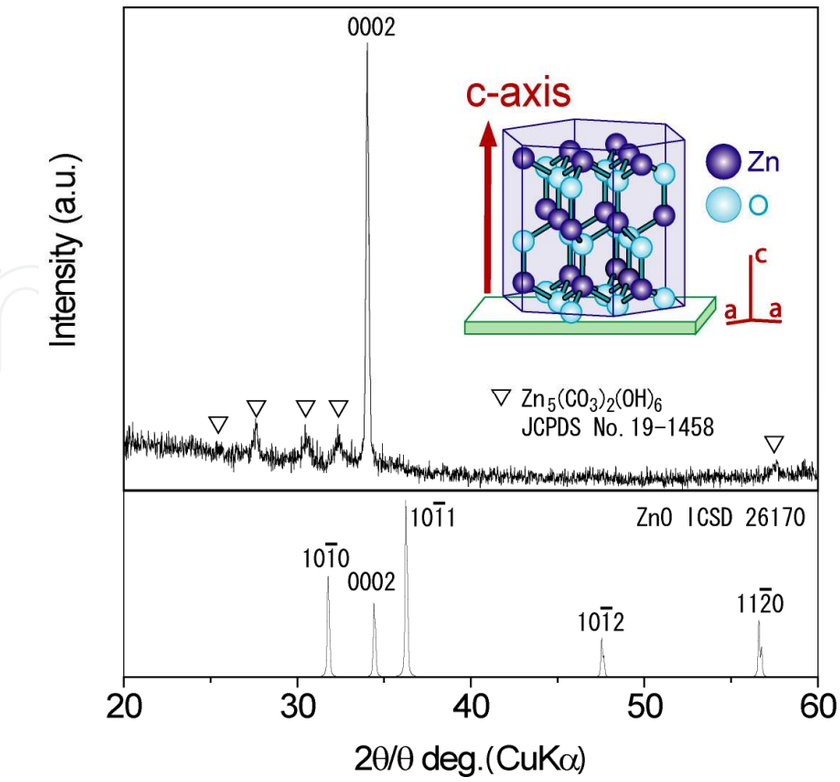

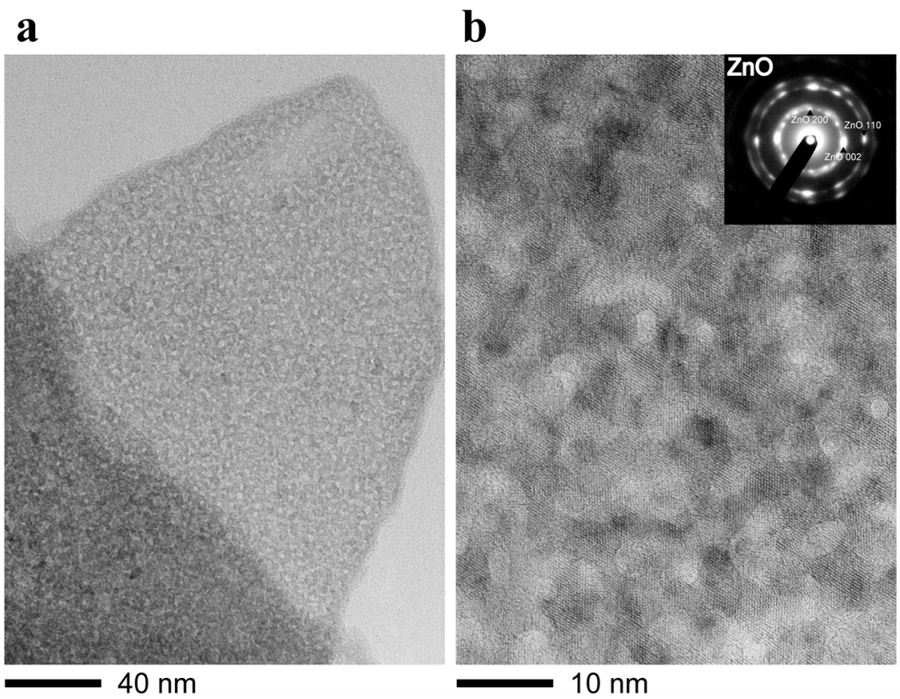

Fig. 2. XRD diffraction pattern of high *c*-axis oriented stand-alone ZnO self-assembled film. (a) TEM micrograph of ZnO nano-sheets. (b) Magnified area of (a). (Insertion) Electron diffraction pattern of ZnO.

The film pasted on a silicon wafer was annealed at 500°C for 1 h in air to evaluate the details of the films. ZnO film maintained its structure during the annealing (Fig. 3). The air side of the film showed a smooth surface (Fig. 3-a1) and the liquid side showed a relief structure having a high specific surface area (Fig. 3-b1, 3-b2). The air side showed the film consisted of dense packing of small ZnO nanosheets and the size of sheets increased toward the liquid-side surface (Fig. 3-a2). ZnO sheets would grow from the air side to the liquid side, i.e., the sheets would nucleate at the liquid-air interface and grow down toward the bottom of the solution by the supply of Zn ions from the solution. Annealed film showed X-ray diffractions of ZnO and Si substrate with no additional phases. As-deposited ZnO nano-sheets were shown to be crystalline ZnO because the sheets maintained their fine structure during the annealing without any phase transition. High *c*-axis orientation was also maintained during the annealing, showing a very strong 0002 diffraction peak.

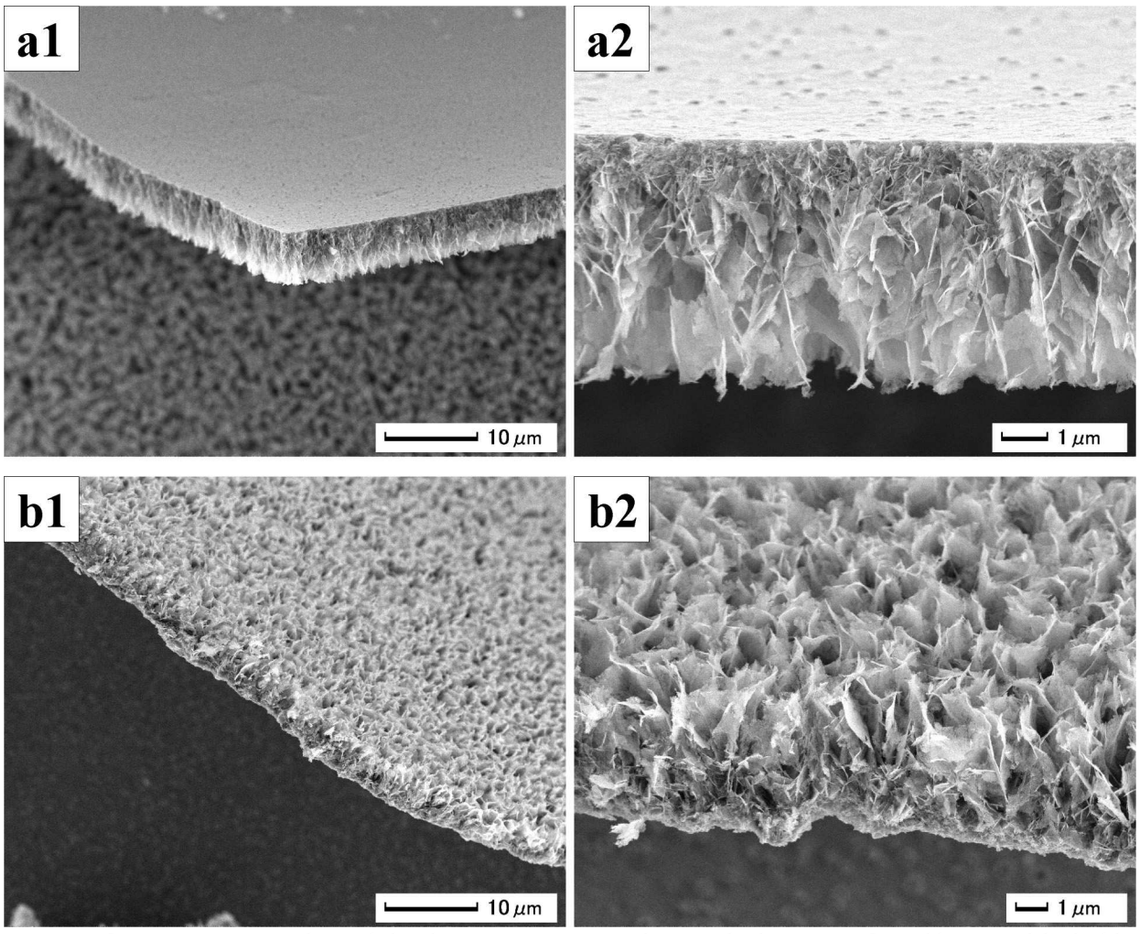

Fig. 3. SEM micrographs of high *c*-axis oriented stand-alone ZnO self-assembled film annealed at 500°C for 1 h in air. (a1) Fracture edge-on profile of ZnO film from air side. (a2) Cross-section profile of ZnO film from air side. (b1) Fracture edge-on profile of ZnO film from liquid side. (b2) Cross-section profile of ZnO film from liquid side.

The solution was further kept at 25°C for 1 month to evaluate the details of the deposition mechanism. The film prepared at the air-liquid interface for 1 month was not hexagonal ZnO. The film showed strong X-ray diffractions of zinc carbonate hydroxide single phase. ZnO would be dissolved by decrease in pH. ZnO would be crystallized at the initial reaction stage for the first 48 h. ZnO was then gradually etched and dissolved by nitric acid and zinc carbonate hydroxide was crystallized using Zn ions which were supplied by the dissolution of crystalline ZnO.

In summary, nano-sheet assembled stand-alone ZnO film was successfully fabricated using a simple solution process. Air-liquid interface was used as a template to form the films. The film had high *c*-axis orientation and showed a strong 0002 diffraction peak and weak 0004 peak. The air side of the film had a flat surface, whereas the liquid side had a rough surface having many ultra-fine spaces surrounded by ZnO nano-sheets. The rough surface of the liquid side was suitable for sensors or dye-sensitized solar cells. The film was also pasted on a desired substrate such as PET films, Si substrate or glass plates. The surface of low heat-resistant flexible polymer film was modified with high *c*-axis oriented crystalline ZnO film without heat treatment. This low-cost, low-temperature technique can be used for a wide range of applications including sensors, solar cells, electrical devices and optical devices using the various properties of high *c*-axis oriented crystalline ZnO.

2.2 Morphology Control of Nanocrystal Assembled TiO_2 Particles[2]

TiO_2 particles were prepared in aqueous solutions at ordinary temperature. The particles were assemblies of nanocrystals that had acicular shape. They had high surface area of 270 m^2/g and unique morphology. They are candidate material for dye-sensitized solar cells and photo catalyst.

Ammonium hexafluorotitanate (12.372 g) and boric acid (11.1852 g) were dissolved in deionized water (600 mL) at 50°C[2]. Concentration of them were 0.15 and 0.05 M, respectively. The solution was kept at 50°C for 30 min using a water bath with no stirring. The solution was centrifuged at 4000 rpm for 10 min (Model 8920, Kubota Corp.). Precipitated particles were dried at 60°C for 12 h after removal of supernatant solution.

The solution became clouded about 10 min after mixing ammonium hexafluorotitanate solution and boric acid solution. The particles were homogeneously nucleated in the solution, turning the solution white.

X-ray diffraction analysis indicated that the particles were single phase of anatase TiO_2. The peaks were observed at 2θ = 25.1, 37.9, 47.6, 54.2, 62.4, 69.3, 75.1, 82.5 and 94.0°. They were assigned to the 101, 004, 200, 105 + 211, 204, 116 + 220, 215, 303 + 224 + 312 and 305 + 321 diffraction peaks of anatase TiO_2 (JCPSD No. 21-1272, ICSD No. 9852) (Fig. 4).

The 004 diffraction intensity of randomly oriented particles is usually 0.2 times the 101 diffraction intensity as shown in JCPDS data (No. 21-1272). However, the 004 diffraction intensity of the particles deposited in our process was 0.36 times the 101 diffraction intensity. Additionally, the integral intensity of the 004 diffraction was 0.18 times the 101 diffraction intensity, indicating the *c*-axis orientation of the particles. Particles were not oriented on the glass holder for XRD measurement. Therefore, TiO_2 crystals would be an anisotropic shape in which the crystals were elongated along the *c*-axis. The crystals would

have a large number of stacks of c planes such as (001) planes compared to stacks of (101) planes. The diffraction intensity from the (004) planes would be enhanced compared to that from the (101) planes.

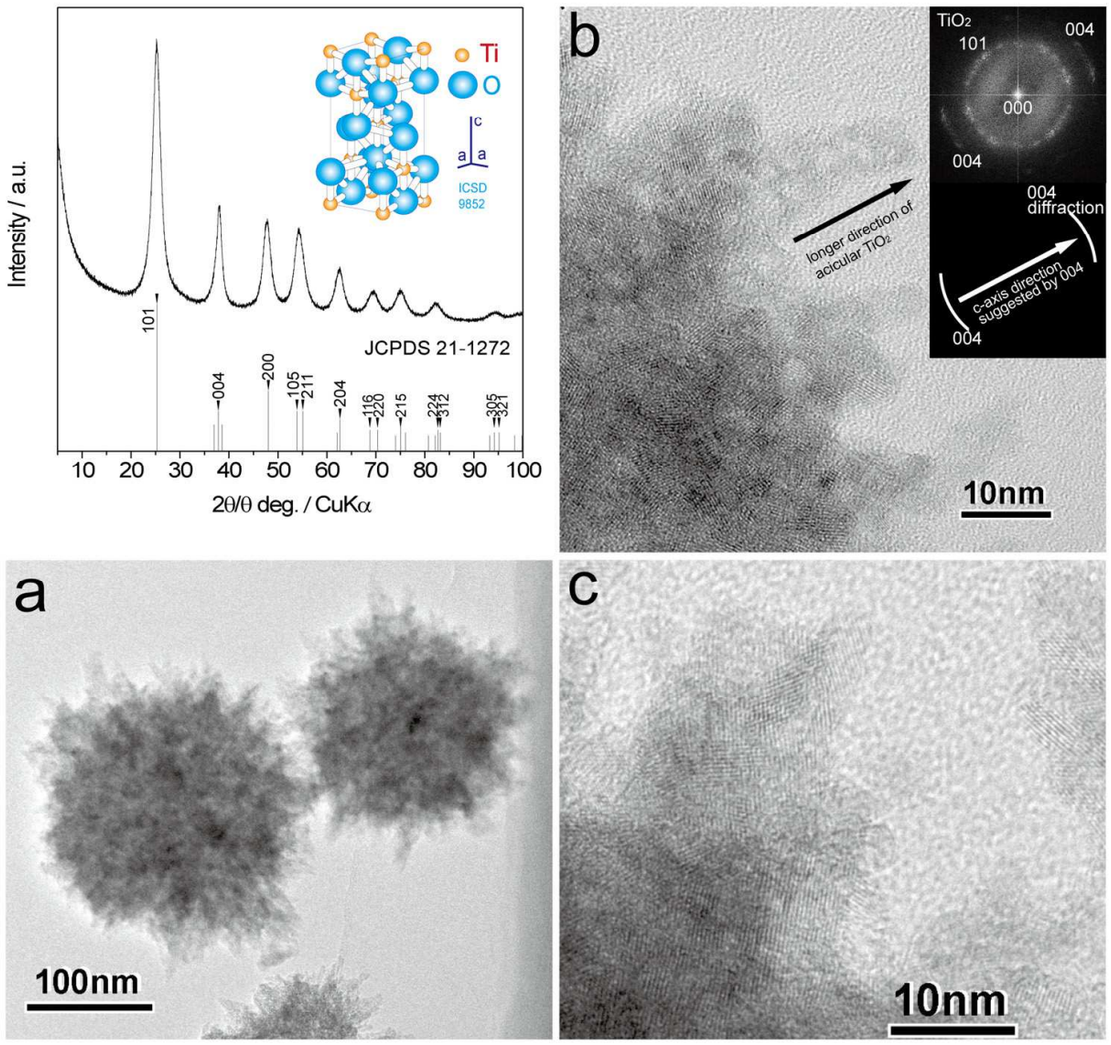

Fig. 4. XRD diffraction pattern of anatase TiO_2 particles. (a): TEM micrograph of anatase TiO_2 particles. (b): Magnified area of (a) showing morphology of acicular crystals. Insertion in (b): FFT image of (b) anatase TiO_2. (c): Magnified area of (a) showing lattice images of anatase TiO_2.

Crystallite size perpendicular to the (101) or (004) planes was estimated from the full-width half-maximum of the 101 or 004 peak to be 3.9 nm or 6.3 nm, respectively. Elongation of crystals in the *c*-axis direction was also suggested by the difference in crystallite size.
The particles were shown to be assemblies of nano TiO_2 crystals (Fig. 4a). Particle diameter was estimated to be 100–200 nm. Relief structures had formed on the surfaces and open pores had formed inside because the particles were porous assemblies of nanocrystals.

Nanocrystals were shown to have acicular shapes (Fig. 4b). They were about 5–10 nm in length. The longer direction of acicular TiO_2 is indicated by the black arrow. The inserted FFT image shows the 101 and 004 diffractions of anatase TiO_2. Nanocrystals are assigned to the single phase of anatase TiO_2. It is notable that the diffraction from the (101) planes has a ring shape due to random orientation but that from the (004) planes was observed only in the upper right region and lower left region in the FFT image. Anisotropic 004 diffractions indicated the direction of the *c*-axis, which was perpendicular to the (004) planes, as shown by the white arrow. It was roughly parallel to the longer direction of acicular TiO_2. These results suggest that acicular TiO_2 grew along the *c*-axis to enhance the diffraction intensity from the (004) planes. Crystal growth of anatase TiO_2 along the *c*-axis was previously observed in TiO_2 films[7]. Anisotropic crystal growth is one of the features of liquid phase crystal deposition.

Acicular nanocrystals showed lattice images of anatase TiO_2 (Fig. 4c). They were constructed of anatase TiO_2 crystals without amorphous or additional phases. Anatase crystals were not covered with amorphous or additional phases even at the tips. Bare anatase crystal with nanosized structure is important to achieve high performance for catalysts and devices.

Crystallization of TiO_2 was effectively utilized to form assemblies of acicular nanocrystals in the process. Open pores and surface relief structures were successfully formed on the particles.

The dried particles were dispersed in water to evaluate zeta potential and particle size distribution after evaluation of N_2 adsorption. The particles had positive zeta potential of 30.2 mV at pH 3.1, which decreased to 5.0, −0.6, −11.3 and −36.3 mV at pH 5.0, 7.0, 9.0 and 11.1, respectively. The isoelectric point was estimated to be pH 6.7, slightly higher than that of anatase TiO_2 (pH 2.7–6.0)[8]. Zeta potential is very sensitive to the particle surface conditions, ions adsorbed on the particle surfaces, and the kind and concentration of ions in the solution. The variations in zeta potential were likely caused by the difference in the surface conditions of TiO_2 particles, affected by the interaction between particles and ions in the solution.

Mean particle size was estimated to be ~550 nm in diameter with a standard deviation (STD) of 220 nm at pH 3.1. This was larger than that observed by TEM. Slight aggregation occurred at pH 3 because the particles were dried completely prior to measurement. Particle size increased with pH and showed a maximum of near the isoelectric point (550 nm at pH 3.1, 3150 nm at pH 5, 4300 nm at pH 7, 5500 nm at pH 9 or 2400 nm at pH 11.1). Strong aggregation resulted from the lack of repulsion force between particles near the isoelectric point.

The particles were generated in the solution at pH 3.8 in this study. It would be suitable to obtain repulsion force between particles for crystallization without strong aggregation.

TiO_2 particles exhibited N_2 adsorption-desorption isotherms of Type IV (Fig. 5a). The desorption isotherm differed from adsorption isotherm in the relative pressure (P/P_0) range from 0.4 to 0.7, showing mesopores in the particles. BET surface area of the particles was estimated to be 270 m^2/g (Fig. 5b). This is higher than that of TiO_2 nanoparticles such as Aeroxide P25 (BET 50 m^2/g, 21 nm in diameter, anatase 80% + rutile 20%, Degussa), Aeroxide P90 (BET 90–100 m^2/g, 14 nm in diameter, anatase 90% + rutile 10%, Degussa), MT-01 (BET 60 m^2/g, 10 nm in diameter, rutile, Tayca Corp.) and Altair TiNano (BET 50 m^2/g, 30–50 nm in diameter, Altair Nanotechnologies Inc.)[9]. A high BET surface area cannot be obtained from particles having a smooth surface even if the particle size is less

than 100 nm. A high BET surface area would be realized by the unique morphology of TiO_2 particles constructed of nanocrystal assemblies.

Total pore volume and average pore diameter were estimated from pores smaller than 230 nm at P/Po = 0.99–0.431 cc/g and 6.4 nm, respectively. They were estimated to be 0.212 cc/g and 3.1 nm, respectively, from pores smaller than 11 nm at P/Po = 0.80. Total pore volume was also estimated by the BJH method from pores smaller than 154 nm to be 0.428 cc/g. Average pore diameter was estimated to be 6.3 nm using BET surface area.

Pore size distribution was calculated by the BJH method using adsorption isotherms (Fig. 5c). It showed a pore size distribution curve having a peak at ~2.8 nm and pores larger than 10 nm. TiO_2 particles would have mesopores of ~2.8 nm surrounded by nanocrystals. Pores larger than 10 nm are considered to be interparticle spaces. The pore size distribution also suggested the existence of micropores smaller than 1 nm.

Pore size distribution was further calculated by the DFT/Monte-Carlo method. The model was in fair agreement with adsorption isotherms (Fig. 5d). Pore size distribution showed a peak at ~3.6 nm that indicated the existence of mesopores of ~3.6 nm (Fig. 5e). The pore size calculated by the DFT/Monte-Carlo method was slightly larger than that calculated from the BJH method because the latter method is considered to have produced an underestimation[10-12]. The pore size distribution also suggested the existence of micropores of ~1 nm, probably resulting from microspaces surrounded by nanocrystals and the uneven surface structure of nanocrystals.

The particles were shown to have a large surface area as well as micropores of ~1 nm, mesopores of ~2.8–3.6 nm and pores larger than 10 nm, by N_2 adsorption characteristics. Assembly of acicular nanocrystals resulted in unique features and high surface area.

TiO_2 particles were generated in the solutions at 90°C for 1h using an oil bath with no stirring for comparison. The solutions became clouded after the addition of boric acid solutions into ammonium hexafluorotitanate solutions. High temperature accelerated crystal growth of TiO_2. Hydrogen chloride of 0.6 ml was added into the solutions of 200ml to decrease crystallization speed of TiO_2. The pH of the solutions was 2.4 one hour after mixing the solutions. BET surface area of the particles was estimated to 18 m^2/g. This is much lower than that of the particles prepared at 50°C and slightly lower than that prepared at 90°C for 8 min in our previous work (44 m^2/g)[13]. Formation of TiO_2 was accelerated at high temperature and it decreased surface area. The particles grew in the solutions to decrease surface area as function of time. Crystallization of TiO_2 was shown to be strongly affected by growth conditions such as solution temperature and growth time.

In summary, anatase TiO_2 particles, 100–200 nm in diameter, were successfully fabricated in aqueous solution. They were assemblies of nanocrystals 5–10 nm that grew anisotropically along the *c*-axis to form acicular shapes. The particles thus had nanorelief surface structures constructed of acicular crystals. They showed *c*-axis orientation due to high-intensity X-ray diffraction from the (004) crystal planes. The particles had a high BET surface area of 270 m^2/g. Total pore volume and average pore diameter were estimated from pores smaller than 230 nm at P/Po = 0.99–0.43 cc/g and 6.4 nm, respectively. They were also estimated from pores smaller than 11 nm at P/Po = 0.80–0.21 cc/g and 3.1 nm, respectively. BJH and DFT/Monte-Carlo analysis of adsorption isotherm indicated the

existence of pores ~2.8 and ~3.6 nm, respectively. Additionally, the analyses suggested the existence of micropores of ~1 nm. Crystallization and self-assembly of nano TiO_2 were effectively utilized to fabricate nanocrystal assembled TiO_2 particles having high surface area and nanorelief surface structure.

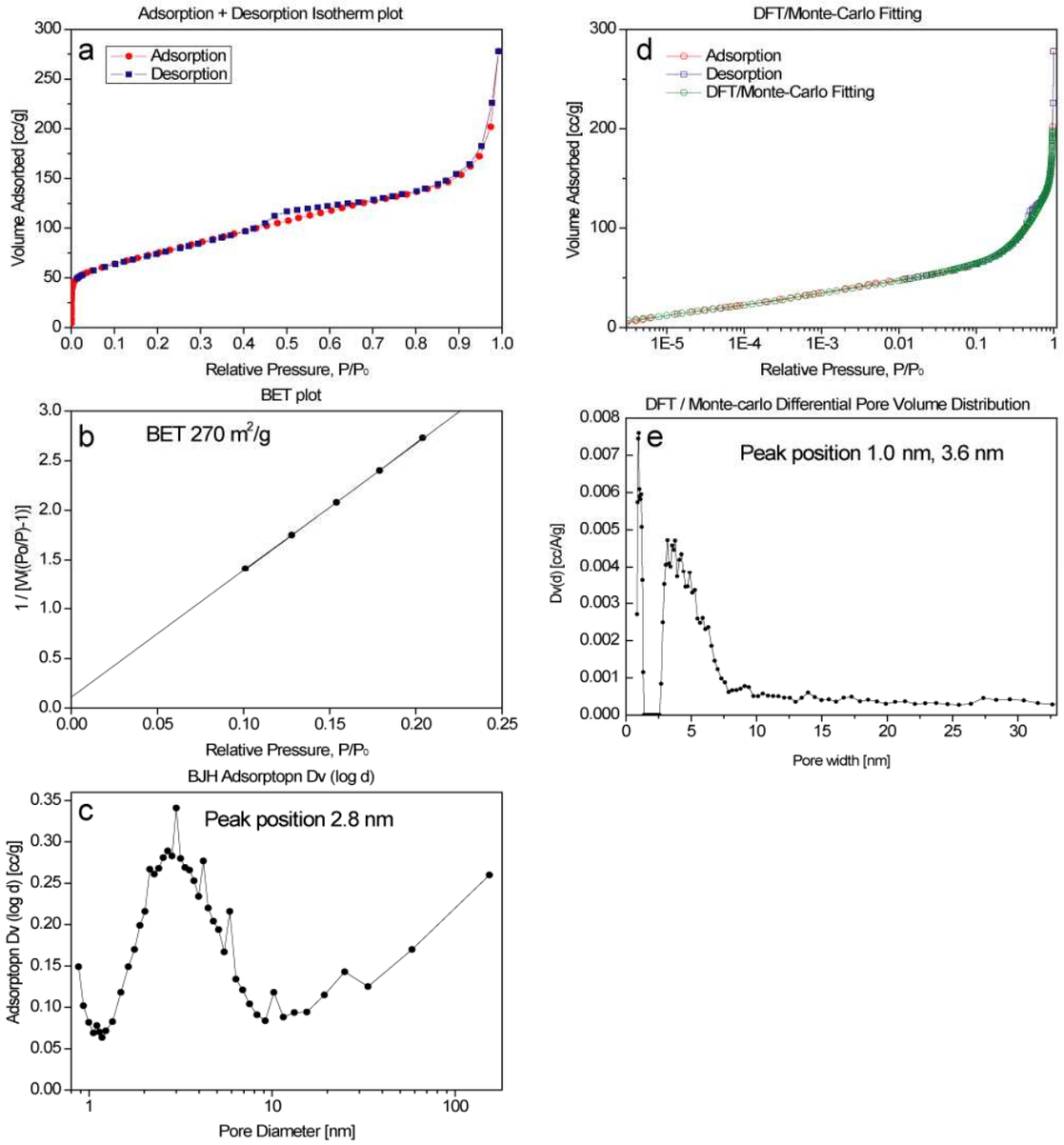

Fig. 5. (a): N_2 adsorption-desorption isotherm of anatase TiO_2 particles. (b): BET surface area of anatase TiO_2 particles. (c): Pore size distribution calculated from N_2 adsorption data of anatase TiO_2 particles using BJH equation. (d): N_2 adsorption-desorption isotherm and DFT/Monte-Carlo fitting curve of anatase TiO_2 particles. (e): Pore size distribution calculated from N_2 adsorption data of anatase TiO_2 particles using DFT/Monte-Carlo equation.

2.3. Morphology Control of Acicular $BaTiO_3$ Particles[3]

Acicular $BaTiO_3$ crystals were fabricated using solution processes. Morphology control of them was realized precise control of crystallization in the solutions.

Oxalic acid (252 mg) was dissolved into isopropyl alcohol (4 ml)[3]. Butyl titanate monomer (0.122 ml) was mixed with the oxalic acid solution, and the solution was then mixed with distilled water (100 ml). The pH of the solution was increased to pH = 7 by adding NaOH (1 M) and distilled water, while the volume of the solution was adjusted to 150 ml by these additions. The aqueous solution (50 ml) with barium acetate (39.3 mg) was mixed with the oxalic acid solution. The mixed solution containing barium acetate (0.77 mM), butyl titanate monomer (2 mM) and oxalic acid (10 mM) was kept at room temperature for several hours with no stirring, and the solution gradually became cloudy. Stirring causes the collision of homogeneously nucleated particles and destruction of large grown particles, and so was avoided in this process. The size of the precipitate was easily controlled from nanometer order to micrometer order by changing the growth period. Large particles were grown by immersion for several hours to evaluate the morphology and crystallinity in detail.

Oxalate ions ($C_2O_4^{2-}$) react with barium ions (Ba^{2+}) to form barium oxalate (BaC_2O_4 $0.5H_2O$). BaC_2O_4 $0.5H_2O$ is dissolved in weak acetate acid provided by barium acetate ($(CH_3COO)_2Ba$), however, it can be deposited at pH 7 which is adjusted by adding NaOH. $BaC_2O_4 \cdot 0.5H_2O$ was thus successfully precipitated from the solution.

Acicular particles were homogeneously nucleated and precipitated from the solution (Fig. 6a). They were on average 23 μm (ranging from 19 to 27 μm) in width and 167 μm (ranging from 144 to 189 μm) in length, giving a high aspect ratio of 7.2. They had sharp edges and clear crystal faces, indicating high crystallinity. A gel-like solid was also coprecipitated from the solution as a second phase.

XRD diffraction patterns for the mixture of acicular particles and gel-like solid showed sharp diffraction peaks of crystalline $BaC_2O_4 \cdot 0.5H_2O$ with no additional phase. Acicular particles were crystalline $BaC_2O_4 \cdot 0.5H_2O$ and the gel-like solid would be an amorphous phase.

Fortunately, $BaC_2O_4 \cdot 0.5H_2O$ has a triclinic crystal structure as shown by the model calculated from structure data [14] (Fig. 6b XRD first step) and thus anisotropic crystal growth was allowed to proceed to produce an acicular shape. Each crystal face has a different surface energy and surface nature such as zeta potential and surface groups. Anisotropic crystal growth is induced by minimizing the total surface energy in ideal crystal growth. Additionally, site-selective adsorption of ions or molecules on specific crystal faces suppresses crystal growth perpendicular to the faces and so induces anisotropic crystal growth. These factors would cause anisotropic crystal growth of $BaC_2O_4 \cdot 0.5H_2O$ and hence allow us to control morphology and fabricate acicular $BaC_2O_4 \cdot 0.5H_2O$ particles. The positions of diffraction peaks corresponded with that of JCPDS No. 20-0134 (Fig. 6b XRD third step) and that calculated from crystal structure data [14] (Fig. 6b XRD second step), however, several diffraction peaks, especially 320 and 201, were enhanced strongly compared to their relative intensity. The enhancement of diffraction intensity from specific crystal faces would be related to anisotropic crystal growth; a large crystal size in a specific

crystal orientation increases the x-ray diffraction intensity for the crystal face perpendicular to the crystal orientation.

EDX elemental analysis indicated the chemical ratio of the precipitate, which included acicular particles and gel-like solid, to be about Ba / Ti = 1 to 1.5. The chemical ratio indicated that the coprecipitated amorphous gel contained Ti ions. Additional Ba ions can be transformed into $BaCO_3$ by annealing and removed by HCl treatment in the next step. The ratio was thus controlled to slightly above Ba / Ti = 1 by adjusting the volume ratio of acicular particles and gel-like solid. Consequently, acicular particles of crystalline $BaC_2O_4 \cdot 0.5H_2O$ with Ti-containing gel-like solid were successfully fabricated in an aqueous solution process.

In comparison, isotropic particles of barium titanyl oxalate ($BaTiO(C_2O_4)_2 \cdot 4H_2O$) were precipitated at pH 2. $TiOC_2O_4$ was formed by the following reaction in which the reaction of oxalic acid ($H_2C_2O_4 \cdot 2H_2O$) with butyl titanate monomer ($(C_4H_9O)_4Ti$) and hydrolysis can take place simultaneously [15].

$(C_4H_9O)_4Ti + H_2C_2O_4 \cdot 2H_2O \rightarrow TiOC_2O_4 + 4C_4H_9OH + H_2O$.....(a)

$TiO(C_2O_4)$ was then converted to oxalotitanic acid ($H_2TiO(C_2O_4)_2$) by the reaction:

$TiO(C_2O_4) + H_2C_2O_4 \cdot 2H_2O \rightarrow H_2TiO(C_2O_4)_2 + 2H_2O$……..(b)

Alcoholic solution containing oxalotitanic acid ($H_2TiO(C_2O_4)_2$) formed by reaction (b) was subjected to the following cation exchange reaction by rapidly adding an aqueous solution of barium acetate at room temperature:

$H_2TiO(C_2O_4)_2 + Ba(CH_3COO)_2 \rightarrow BaTiO(C_2O_4)_2\downarrow + 2CH_3COOH$ (c)

$BaTiO(C_2O_4)_2$ isotropic particles were formed by reaction (c).

On the other hand, neither $BaC_2O_4 \cdot 0.5H_2O$ nor $BaTiO(C_2O_4)_2$ was precipitated at pH 3 to pH 6. Gel-like solid was formed in the solution and their XRD spectra showed no diffraction peaks. The amorphous gel that precipitated at pH = 3 to 6 would be the same as the amorphous gel coprecipitated at pH 7.

These comparisons show that the crystal growth and morphology control of $BaC_2O_4 \cdot 0.5H_2O$ are sensitive to the solution conditions.

The precipitate was annealed at 750 °C for 5 h in air. Acicular $BaC_2O_4 \cdot 0.5H_2O$ particles were reacted with Ti-containing amorphous gel to introduce Ti ions to transform into crystalline $BaTiO_3$. X-ray diffraction of the annealed precipitate showed crystalline $BaTiO_3$ and an additional barium carbonate phase ($BaCO_3$). Excess precipitation of $BaC_2O_4 \cdot 0.5H_2O$ caused the generation of barium carbonate phase ($BaCO_3$) as expected.

The annealed precipitate was further immersed in HCl solution (1 M) to dissolve barium carbonate ($BaCO_3$). Acicular particles of crystalline $BaTiO_3$ were successfully fabricated with no additional phase. Particles showed acicular shape with 2.8×10×50 μm and x-ray diffraction of single-phase crystalline $BaTiO_3$ (Fig. 6c). The high aspect ratio of the particles (17.8 = 50 / 2.8) would be provided by that of $BaC_2O_4 \cdot 0.5H_2O$ particles. The particle size of acicular $BaTiO_3$ can be easily controlled by the growth period and solution concentration for $BaC_2O_4 \cdot 0.5H_2O$ precipitation which decides the particle size of $BaC_2O_4 \cdot 0.5H_2O$.

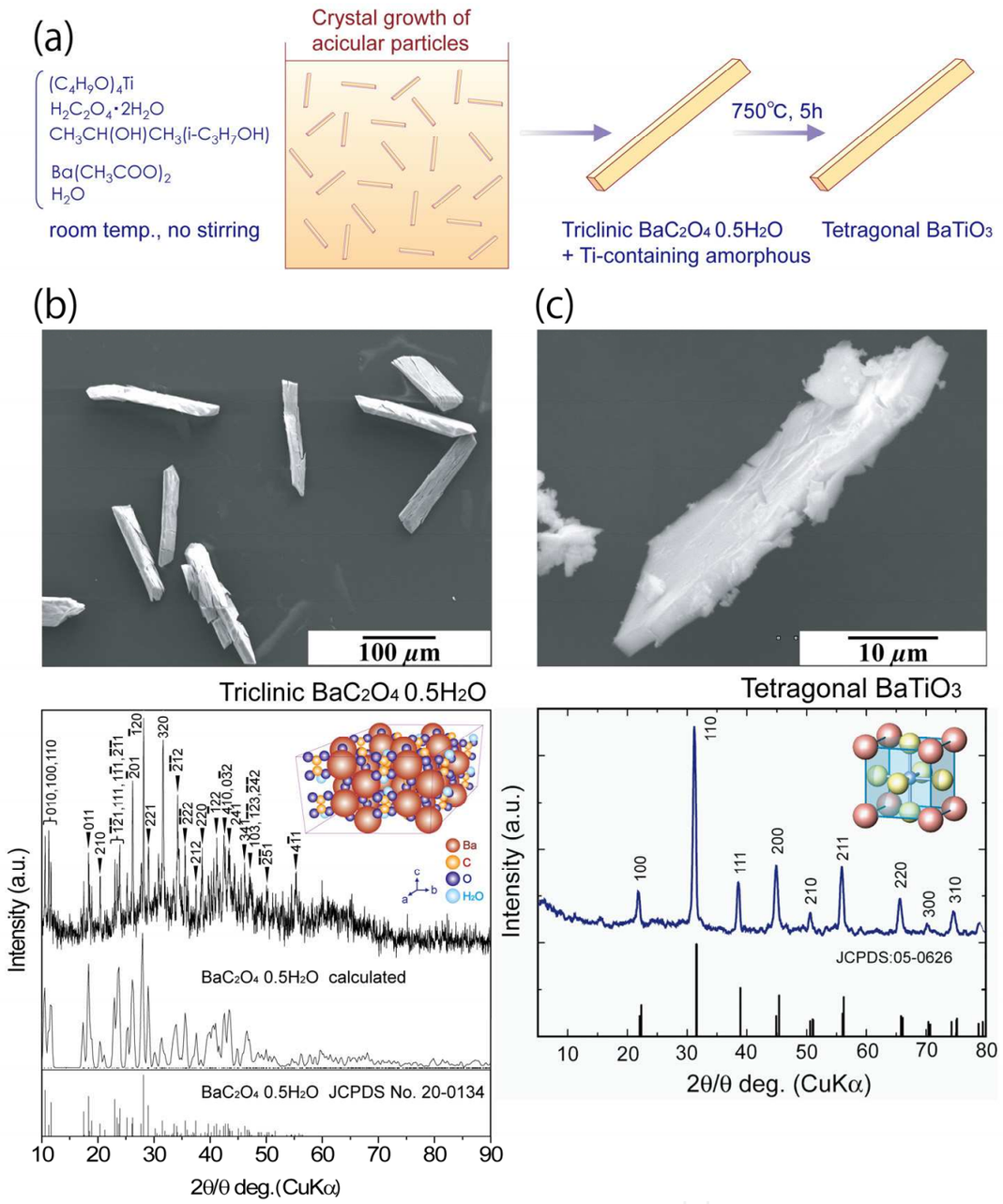

Fig. 6. (a) Conceptual process for fabricating acicular $BaTiO_3$ particles. Morphology control of $BaC_2O_4 \cdot 0.5H_2O$ particles and phase transition to $BaTiO_3$. (b) SEM micrograph and XRD diffraction pattern of acicular $BaC_2O_4 \cdot 0.5H_2O$ particles precipitated from an aqueous solution at pH = 7. XRD diffraction measurement data (first step), XRD pattern calculated from crystal structure data[16] (second step) and XRD pattern of JCPDS No. 20-134 (third step) are shown for triclinic $BaC_2O_4 \cdot 0.5H_2O$. (c) SEM micrograph and XRD diffraction pattern of acicular $BaTiO_3$ particles after annealing at 750 °C for 5 h and HCl treatment. XRD diffraction measurement data (first step) and XRD pattern of JCPDS No. 05-0626 (second step) are shown for tetragonal $BaTiO_3$.

$BaTiO_3$ has a cubic crystal structure at high temperature above phase transition and has a tetragonal crystal structure at room temperature. The cubic crystal structure is completely isotropic and the tetragonal crystal structure results from stretching a cubic lattice along one of its lattice vectors. For both of the crystal structures it is difficult to control anisotropic crystal growth, however, with our newly developed process we could successfully control the morphology and fabricate acicular particles. This was achieved by controlling the morphology of triclinic $BaC_2O_4 \cdot 0.5H_2O$ to acicular shape and the phase transition to $BaTiO_3$ by introducing Ti ions from the coprecipitated amorphous phase. The novel concept can be applied to a wide variety of morphology control and crystal growth control for advanced electronic devices composed of crystalline materials.

In summary, a novel process to fabricate acicular $BaTiO_3$ particles was developed. Morphology control of crystalline $BaC_2O_4 \cdot 0.5H_2O$ to acicular shape was realized in an aqueous solution. The particles were then transformed into crystalline $BaTiO_3$ by introducing Ti ions from the coprecipitated amorphous gel phase during the annealing process. Consequently, acicular particles of tetragonal $BaTiO_3$ were produced by combining several key technologies. Morphology control in this system has high scientific value for crystal growth, and acicular particles of crystalline $BaTiO_3$ may have a great impact on ultra-thin MLCC in future.

3. Liquid Phase Site-selective Deposition of Metal Oxide Nanocrystals

3.1. Site-selective Deposition of Anatase TiO_2[4]

Site-selective deposition of anatase TiO_2 nanocrystals was achieved in aqueous solutions. Nucleation and crystal growth of TiO_2 were accelerated on super hydrophilic surfaces. It allowed us to form micro-patterns of TiO_2 nanocrystals.

Transparent conductive substrate of F doped SnO_2 (FTO, SnO_2: F, Asahi Glass Co., Ltd., 9.3-9.7 Ω/□, 26 × 50 × 1.1 mm) was blown by air to remove dust and was exposed to ultraviolet light (low-pressure mercury lamp PL16-110, air flow, 100 V, 200 W, SEN Lights Co.) for 10 min through a photomask (Test-chart-No.1-N type, quartz substrate, 1.524 mm thickness, Toppan Printing Co., Ltd.) (Fig. 7)[4]. The initial SnO_2: F substrate showed a water contact angle of 96°. The UV-irradiated surface was, however, wetted completely (contact angle 0–1°). The contact angle decreased with irradiation time (96°, 70°, 54°, 35°, 14°, 5° and 0° for 0 min, 0.5 min, 1 min, 2 min, 3 min, 4 min and 5 min, respectively). This suggests that a small amount of adsorbed molecules on the SnO_2: F substrate was removed completely by UV irradiation. The surface of the SnO_2: F substrate would be covered by hydrophilic OH groups after irradiation. Consequently, the SnO_2: F substrate was modified to have a patterned surface with hydrophobic regions and super-hydrophilic regions.

Ammonium hexafluorotitanate ($[NH_4]_2TiF_6$) (2.0620 g) and boric acid (H_3BO_3) (1.8642 g) were separately dissolved in deionized water (100 mL) at 50°C. Boric acid solution was added to ammonium hexafluorotitanate solution at concentrations of 0.15 M and 0.05 M, respectively. The SnO_2: F substrate having a patterned surface with hydrophobic regions and super-hydrophilic regions was covered by a silicon rubber sponge sheet (Silico-sheet, SR-SG-S 5mmt RA grade, Shin-etsu Finetech Co., Ltd.) to suppress deposition of TiO_2 at the initial stage. The substrate was immersed perpendicularly in the middle of the solution

(Fig. 7). The solution was kept at 50°C with no stirring. The silicon rubber sponge sheet was removed from the SnO_2: F substrate after 25 h, then the substrate was kept for a further 2 h at 50°C. The substrate was covered by the sheet instead of immersion of substrate at 25h to avoid agitation of the solution.

The solution became clouded in about 10 min after the mixing of ammonium hexafluorotitanate solution and boric acid solution. The particles were homogeneously nucleated in the solution and made the solution white. They then gradually precipitated and fell to the bottom of the vessel, so the solution became transparent over a period of hours. Ti ions were consumed for crystallization of TiO_2 particles, thus decreasing the ion concentration in the solution. The super-saturation degree of the solution was sufficiently low to realize slow heterogeneous nucleation without homogeneous nucleation which forms TiO_2 particles. The silicon rubber sponge sheet was removed from the SnO_2: F substrate after 25 h, then the substrate was kept for a further 2 h at 50°C. Consequently, the patterned surface on the SnO_2: F substrate was exposed to the transparent solution including Ti ions at a low concentration for 2 h. Heterogeneous nucleation and slow crystallization of TiO_2 progressed only on the substrate.

Deposition of anatase TiO_2 proceeds by the following mechanisms[7]:

$$TiF_6^{2-} + 2H_2O \rightleftharpoons TiO_2 + 4H^+ + 6F^- \quad \cdots(a)$$

$$BO_3^{3-} + 4F^- + 6H^+ \longrightarrow BF_4^- + 3H_2O \quad \cdots(b)$$

Equation (a) is described in detail by the following two equations:

$$TiF_6^{2-} \xrightarrow{nOH^-} TiF_{6-n}(OH)_n^{2-} + nF^- \xrightarrow{(6-n)OH^-} Ti(OH)_6^{2-} + 6F^- \quad \cdots(c)$$

$$Ti(OH)_6^{2-} \longrightarrow TiO_2 + 2H_2O + 2OH^- \quad \cdots(d)$$

Fluorinated titanium complex ions gradually change into titanium hydroxide complex ions in an aqueous solution as shown in Eq. (c). The increase of F^- concentration displaces Eqs. (a) and (c) to the left, however, the produced F^- can be scavenged by H_3BO_3 (BO_3^{3-}) as shown in Eq. (b) to displace Eqs. (a) and (c) to the right. Anatase TiO_2 formed from titanium hydroxide complex ions ($Ti(OH)_6^{2-}$) in Eq. (d).

Liquid phase patterning was not realized in the initial solution but realized in the solution after 25 h. Solution condition was evaluated as function of time to clarify this reason. The solution was transparent immediately after the mixing of ammonium hexafluorotitanate solution and boric acid solution, became clouded after 0.5 h and showed maximum whiteness after 1 h. Anatase TiO_2 particles nucleated homogeneously in the solution and grew to form large particles, which gradually precipitated and made the bottom of the vessel white. The solution became slightly white after 5 h and transparent after 25 h. The solutions changed to transparent by the filtrations. Precipitated particles from the residual solution and particles from the supernatant solution trapped by filters were determined by XRD evaluation to be a single phase of anatase TiO_2.

Precipitated particles from the residual solution increased as 0 mg, 165.1 mg, 230.9 mg and 424.4 mg at 0 h, 2 h, 5 h and 25 h, respectively. The precipitation increased rapidly at the initial stage and moderately after 2 h, reflecting the decrease of crystal growth rate.
The weight of particles > 2.5 μm in diameter was estimated to be 2.8 mg, 49.7 mg, 9.5 mg, 0 mg and 0 mg at 0.5 h, 1 h, 2 h, 5 h and 25 h, respectively. Particles were formed at the initial stage and precipitated, making the bottom of the vessel white. This is consistent with the color change of the solution.
The precipitate from the filtrate collected by all of the filters was evaluated by XRD. The white powder contained anatase TiO_2, rutile TiO_2 and a large amount of boric acid. These were crystallized from ions in the filtrate during drying. The weight was estimated to be 1455 mg, 1429 mg, 1392 mg, 1345 mg and 1341 mg at 0.5 h, 1 h, 2 h, 5 h and 25 h, respectively. This indicated that the solution contained a high concentration of ions at the initial stage, which then decreased as a function of time. Ion concentration would decrease by the crystallization and precipitation of anatase TiO_2. This result is consistent with the weight variation of precipitated particles, weight variation of suspended particles and solution color change shown in the photographs.
Liquid phase patterning was not realized in the initial clouded solution but realized in the transparent solution after 25 h. Evaluation of solution condition as function of time showed the reason of this phenomenon. TiO_2 particles formed at the initial stage around 1 h and precipitated gradually. Ions were consumed for crystallization of TiO_2 and decreased as a function of time. Heterogeneous nucleation predominantly progressed after 5 h. Consequently, TiO_2 was formed on super hydrophilic regions selectively to realize liquid phase patterning.
FTO substrate was immersed in the solution for 25 h to form a thick film and ultrasonicated in water for 20 min. TiO_2 film was constructed of two layers. Under layer with 200 nm thickness was a polycrystalline film of anatase TiO_2. Upper layer with 300 nm thickness was an assembly of acicular TiO_2 crystals which grew perpendicular to the substrate. The film was shown by electron diffraction pattern to be a single phase of anatase TiO_2. Electron diffraction from the 004 plane was stronger than that of the 101, 200, 211 planes, etc to show anisotropic crystal growth along the *c*-axis. Additionally, 004 diffractions were strong perpendicular to the substrate, showing that the *c*-axis orientation of acicular crystals was perpendicular to the substrate. The FTO layer was shown to be a single phase of SnO_2 with high crystallinity. Acicular TiO_2 crystals had a long shape, being ~ 300 nm in length and 10 – 100 nm in diameter. A lattice image of anatase TiO_2 was observed from the crystals.
The film deposited on the substrate was evaluated by XRD analysis. Strong X-ray diffractions were observed for films deposited on FTO substrates and assigned to SnO_2 of FTO films. The 004 diffraction peak of anatase TiO_2 was not observed clearly for TiO_2 film on FTO substrates because both of the weak 004 diffraction peak of TiO_2 and the strong diffraction peak of FTO were observed at the same angle. Glass substrates with no FTO coating were immersed in the solution. Weak X-ray diffraction peaks were observed at 2θ = 25.3, 37.7, 48.0, 53.9, 55.1 and 62.7° for the films deposited on glass substrates. They were assigned to 101, 004, 200, 105, 211 and 204 diffraction peaks of anatase TiO_2 (ICSD No. 9852) (Fig. 7). A broad diffraction peak from the glass substrate was also observed at about 2θ = 25°.

The intensity of the 004 diffraction peak was stronger than that of the 101 diffraction peak for the film obtained by the liquid phase crystal deposition method, though the intensity of 101 was stronger than that of 004 for anatase TiO_2 powders with no orientation (ICSD No. 9852). The integral intensity or peak height of 004 was 2.6 times or 2.2 times that of 101, respectively, suggesting high *c*-axis orientation of anatase TiO_2 crystals. Crystallite size perpendicular to the 101 or 004 planes was estimated from the full-width half-maximum of the 101 or 004 peak to be 9 nm or 17 nm, respectively. Elongation of crystals in the *c*-axis direction was also suggested by the difference of crystallite size. These evaluations were consistent with high *c*-axis orientation observed by TEM and electron diffraction. Crystallite size estimated by XRD was similar to that in TiO_2 under layer rather than that of acicular crystals observed by TEM. TiO_2 thin film prepared on a glass would be constructed of not acicular crystals but polycrystals in under layer.

After having been immersed in the solution, the substrate was rinsed with distilled water and dried in air (Fig. 7). The initial FTO surface appeared to be blue-green under white light due to light diffracted from the FTO layer. On the other hand, TiO_2 films deposited on the super-hydrophilic surface appeared to be yellow-green. The color change would be caused by deposition of transparent TiO_2 film which influenced the wavelength of the diffracted light.

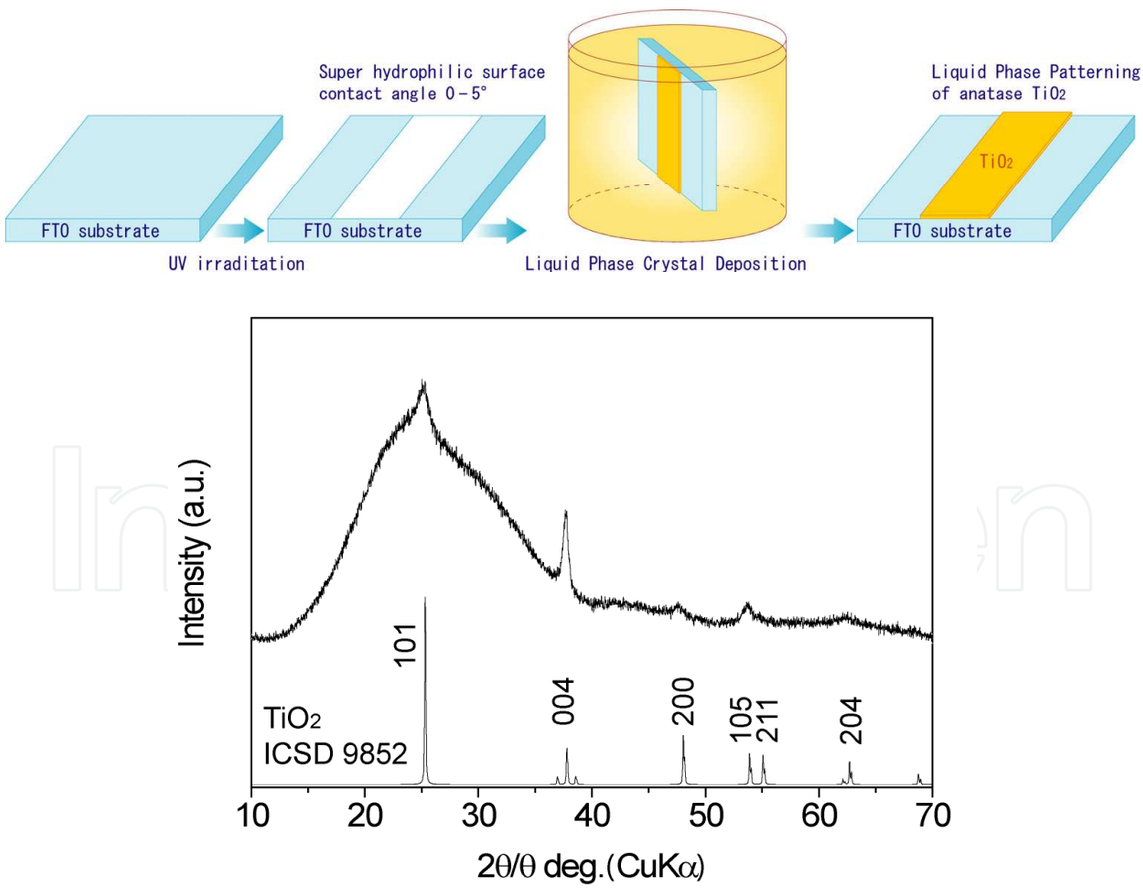

Fig. 7. Conceptual process for liquid phase patterning of anatase TiO_2 films using super-hydrophilic surface. XRD diffraction pattern of anatase TiO_2 film on a glass substrate.

The micropattern of TiO_2 was shown by SEM evaluation to be successfully fabricated (Fig. 8(Top)). TiO_2 deposited on super-hydrophilic regions showed black contrast, while the initial FTO regions without deposition showed white contrast in Fig. 8(top). The average line width in Fig. 8(top) is 55 μm. Line edge roughness[16], as measured by the standard deviation of the line width, is ~2.8 μm. This represents a ~5% variation (i.e., 2.8/55) in the nominal line width, similar to the usual 5% variation afforded by current electronics design rules. The minimum line width of the pattern depends on the resolution of the photomask and wavelength of irradiated light (184.9 nm). It would be improved to ~ 1 μm by using a high-resolution photomask.

The FTO layer was a particulate film having a rough surface (Fig. 8-b1, b2). Edged particles of 100 – 500 nm in diameter were observed on the surface. The micropattern of TiO_2 thin film was covered by an assembly of nano crystals of 10 – 30 nm in diameter (Fig. 8-a1, a2). The nano crystals would be anatase TiO_2 which grew anisotropically. The TiO_2 film also had large structural relief of 100 – 500 nm in diameter. As the thin TiO_2 film was deposited on the edged particulate surface of the FTO layer, the surface of TiO_2 had large structural relief.

The morphology of the TiO_2 layer and FTO layer was further observed by fracture cross section profiles (Fig. 9). The polycrystalline FTO layer prepared on a flat glass substrate was shown to have a thickness of ~ 900 nm, and a high roughness of 100 – 200 nm on the surface (Fig. 9a). Nano TiO_2 crystals were deposited on the super-hydrophilic FTO surface (Fig. 9a), whereas no deposition was observed on the initial FTO surface. The super-hydrophilic FTO surface was covered with an array of nano TiO_2 crystals (Fig. 9b, c), which had a long shape of ~ 150 nm in length and ~ 20 nm in diameter. These observations were consistent with TEM and XRD evaluations. Nano TiO_2 crystals would grow along the *c*-axis and thus enhance the 004 X-ray diffraction peak and 004 electron diffraction peak. They formed a long shape having a high aspect ratio of 7.5 (150 nm in length / 20 nm in diameter) as shown in the SEM fracture cross section profile (Fig. 9b, c) and TEM micrograph. The orientation of nano TiO_2 crystals with their long axis perpendicular to the FTO layer (Fig. 9b, c) would also enhance the 004 diffraction peak.

In summary, a micropattern of anatase TiO_2 thin film was successfully fabricated on an SnO_2: F substrate in an aqueous solution. Crystalline anatase TiO_2 was deposited by liquid phase crystal deposition at 50°C. Nucleation and crystal growth of TiO_2 were accelerated on the super-hydrophilic SnO_2: F surface, but were suppressed on the hydrophobic initial SnO_2: F surface. Consequently, liquid phase patterning of anatase TiO_2 was achieved on an SnO_2: F substrate. TiO_2 crystals were directly deposited on the SnO_2: F surface without any insulating layers which decrease the electrical conductivity between TiO_2 and the SnO_2: F substrate. The micropattern of anatase TiO_2 on the SnO_2: F substrates could be applied to electrodes of dye-sensitized solar cells or molecular sensors. Additionally, this process can be used to form a flexible micropattern of anatase TiO_2 electrodes on low-heat-resistant conductive polymer films. This process will contribute to the microfabrication of TiO_2 electrodes for dye-sensitized solar cells or molecular sensors.

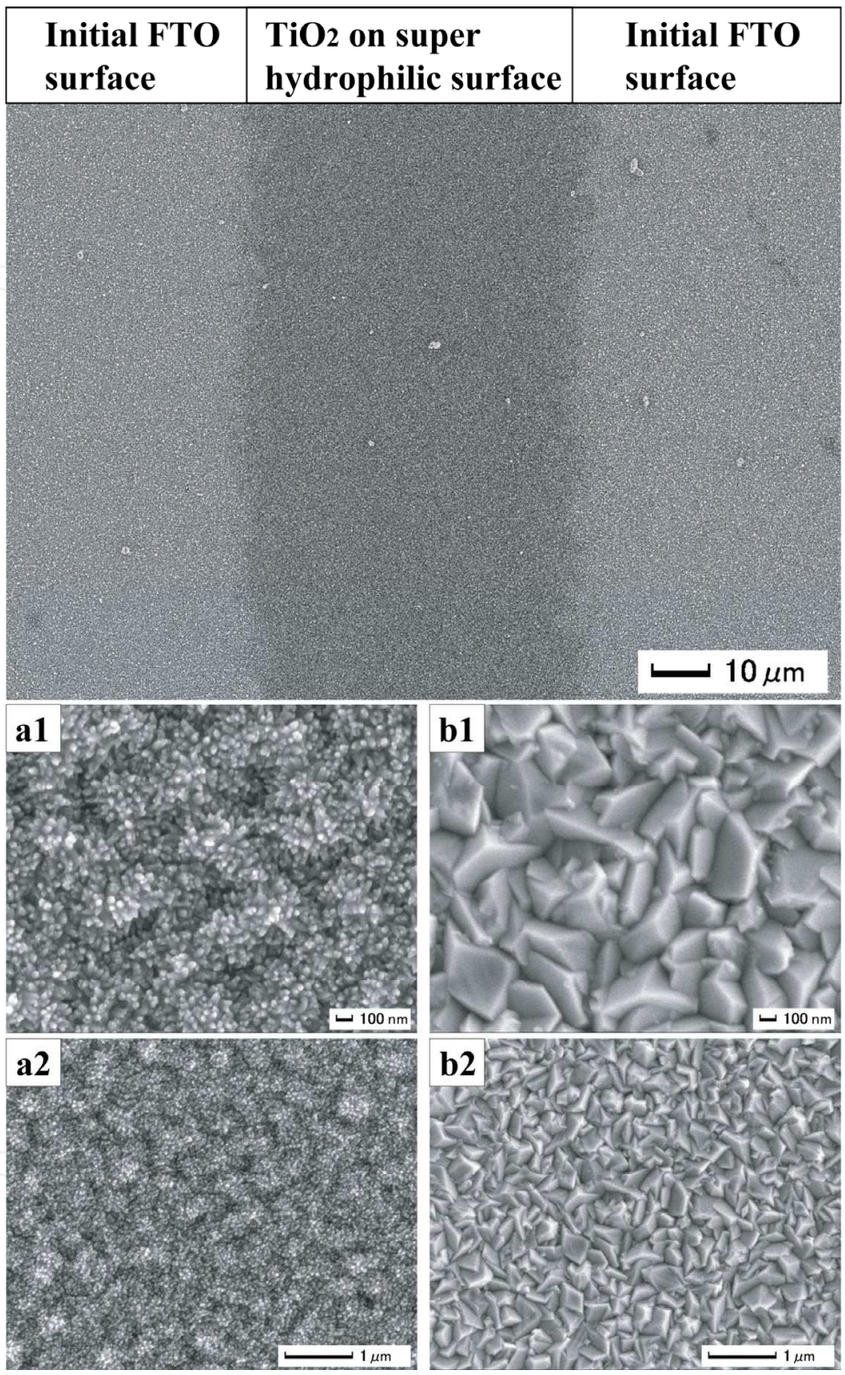

Fig. 8. SEM micrographs of a micropattern of anatase TiO_2 films on SnO_2: F substrates. (Top) Micropattern of anatase TiO_2 films. (a1) Surface of anatase TiO_2 films deposited on super-hydrophilic region. TiO_2 was formed on super-hydrophilic region which was cleaned by UV irradiation before the immersion. (a2) Magnified area of (a1) showing surface morphology of anatase TiO_2 film. (b1) Surface of SnO_2: F substrate without TiO_2 deposition. TiO_2 was not formed on non-cleaned region. (b2) Magnified area of (b1) showing surface morphology of SnO_2: F substrate.

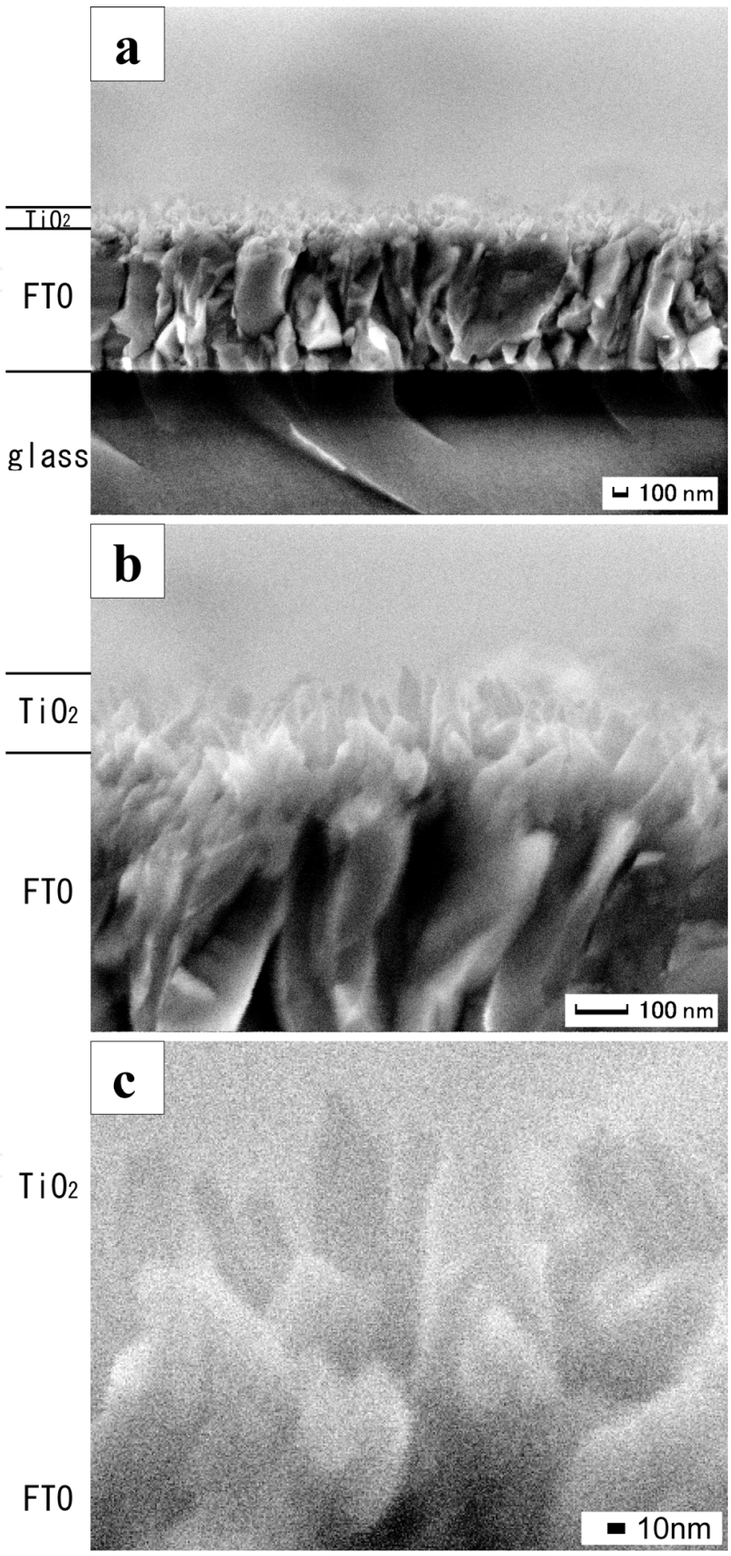

Fig. 9. SEM micrographs of anatase TiO_2 films on SnO_2: F substrates. (a) Fracture cross section of TiO_2 films. (b, c) Magnified area of (a) showing morphology of nano TiO_2 crystals.

3.2. Site-selective Deposition of Eu:Y_2O_3[5]

Micropatterning of Eu doped Y_2O_3 nanocrystals was also realized using site-selective deposition in the solutions. Self-assembled monolayer was utilized as template in this system.
Si substrate (p-type [100], 1–50 Ωcm, Newwingo Co., Ltd.) was cleaned ultrasonically in acetone, ethanol and deionized water for 5 min, respectively, in this order and was exposed to ultraviolet light and ozone gas for 10 min to remove organic contamination by using a UV/ozone cleaner (184.9 nm and 253.7 nm) (low-pressure mercury lamp 200 W, PL21-200, SEN Lights Co., 18 mW/cm^2, distance from lamp 30 mm, 24 °C, humidity 73%, air flow 0.52 m^3/min, 100 V, 320 W)[17-20]. APTS (3-Aminopropyltriethoxysilane)-SAM was prepared by immersing the Si substrate in an anhydrous toluene solution containing 1 vol% APTS for 1 h in N_2 atmosphere. The substrate was rinsed with a fresh anhydrous toluene in N_2 atmosphere. The substrate with SAM was baked at 120 °C for 5 min to remove residual solvent and promote chemisorption of the SAM.
APTS-SAM was then irradiated by ultraviolet light (PL21-200) through a photomask (Test-chart-No.1-N type, quartz substrate, 1.524 mm thickness, guaranteed line width 2 μm ± 0.5 μm, Toppan Printing Co., Ltd.) for 10 min. UV irradiation modified an amino-terminated silane to a silanol forming a pattern of amino-terminated silane regions and silanol regions[17-20]. Patterned APTS-SAM having amino regions and silanol regions was used as a template for patterning of yttrium oxide. Initially deposited APTS-SAM showed water contact angles of 48°. The UV-irradiated surface of SAM was, however, wetted completely (contact angle <5°). This suggests that SAM of APTS was modified to hydrophilic OH group surfaces by UV irradiation.
The patterned APTS-SAM was immersed in an aqueous solution containing $Y(NO_3)_3 \cdot 6H_2O$ (4 mM), $Eu(NO_3)_3 \cdot 6H_2O$ (0.4 mM) and NH_2CONH_2 (50 mM) at 25 °C[5]. The solution was heated to 77 °C gradually as shown in Fig. 10 since urea (NH_2CONH_2) decomposes to form ammonium ions (NH_4^+) above 70 °C (Eq. (a)). The decomposition of urea at elevated temperature plays an essential role in the deposition of yttrium oxide. The aqueous solution of urea yields ammonium ions and cyanate ions (OCN^-) at temperatures above 70 °C[21] (Eq. (a)). Cyanate ions react rapidly according to Eq. (b). Yttrium ions are weakly hydrolyzed[22,23] in water to $YOH(H_2O)_n^{2+}$ (Eq. (c)). The resulting release of protons (H^+) and/or hydronium ions (H_3O^+) accelerates urea decomposition (Eq. (b)). The precipitation of the amorphous basic yttrium carbonate ($Y(OH)CO_3 \cdot xH_2O$, x=1) can take place through the reaction in Eq. (d)[24,25]. The controlled release of cyanate ions by urea decomposition causes deposition of basic yttrium carbonate once the critical supersaturation in terms of reacting component is achieved. Since the decomposition of urea is quite slow, the amount needed to reach supersaturation within a given period of time must be considerably higher than the stoichiometric amount of yttrium ions, as revealed by previous studies of lanthanide compounds[26].
The temperature of the solution increased gradually and reached 77 °C in about 80 min[5]. The solution was kept at ~ 77 °C during deposition. The pH of the solution increased from 5.2 to 5.8 in about 90 min and then gradually decreased to 5.6. Temperature and pH increased for the initial 90 min and became stable after 90 min. The average size of particles homogeneously nucleated in the solution at 100 min was about 227 nm and increased to 262 nm at 150 min, 282 nm at 180 min, 310 nm at 210 min, and 323 nm at 240 min (Fig. 10a). Particles nucleated and grew after the solution temperature exceeded 70 °C because urea

decomposes above 70 °C to form carbonate ions[21] which causes deposition of basic yttrium carbonate[23-26]. The particles grew rapidly at the beginning of the growth period and then their growth rate decreased exponentially (Fig. 10a). The decrease in growth rate was caused by the decrease of supersaturation degree influenced by a decrease in solution concentration.

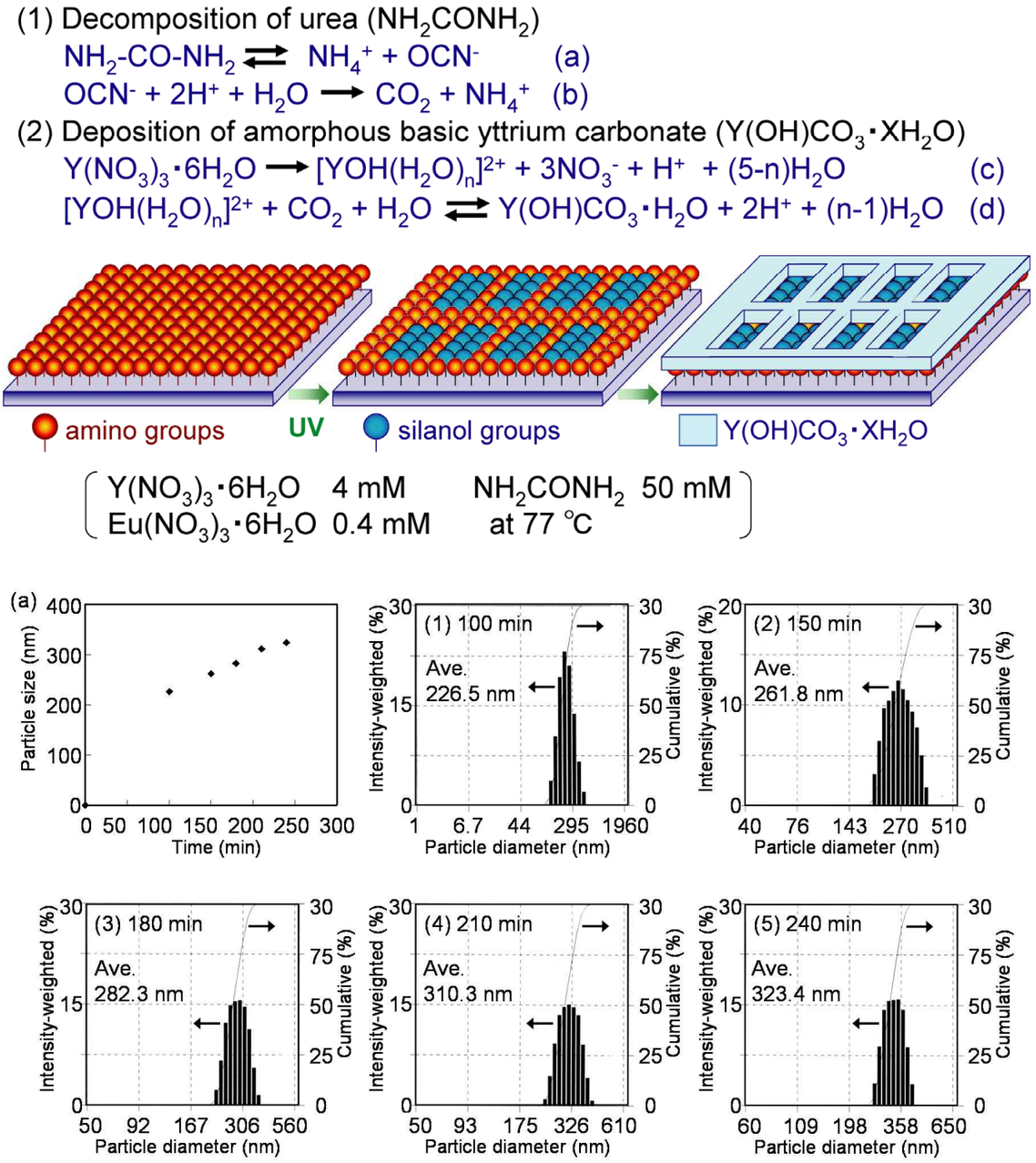

Fig. 10. Conceptual process for site-selective deposition of visible-light emitting Y_2O_3:Eu thin films using a self-assembled monolayer. (a) Time variation of particle size distribution. (1-5) Particle size distribution of yttrium carbonate particles at (1) 100 min, (2) 150 min, (3) 180 min, (4) 210 min or (5) 240 min.

Yttrium carbonate films were observed to deposit on amino regions of a patterned SAM after the immersion in an aqueous solution (Fig. 11A, B). Deposits showed white contrast, while silanol regions without deposition showed black contrast in SEM observation. Narrow lines of depositions having 10–50 μm width were successfully fabricated in an aqueous solution. Patterned APTS-SAM showed high ability for site-selective deposition of yttrium carbonate in solution systems.

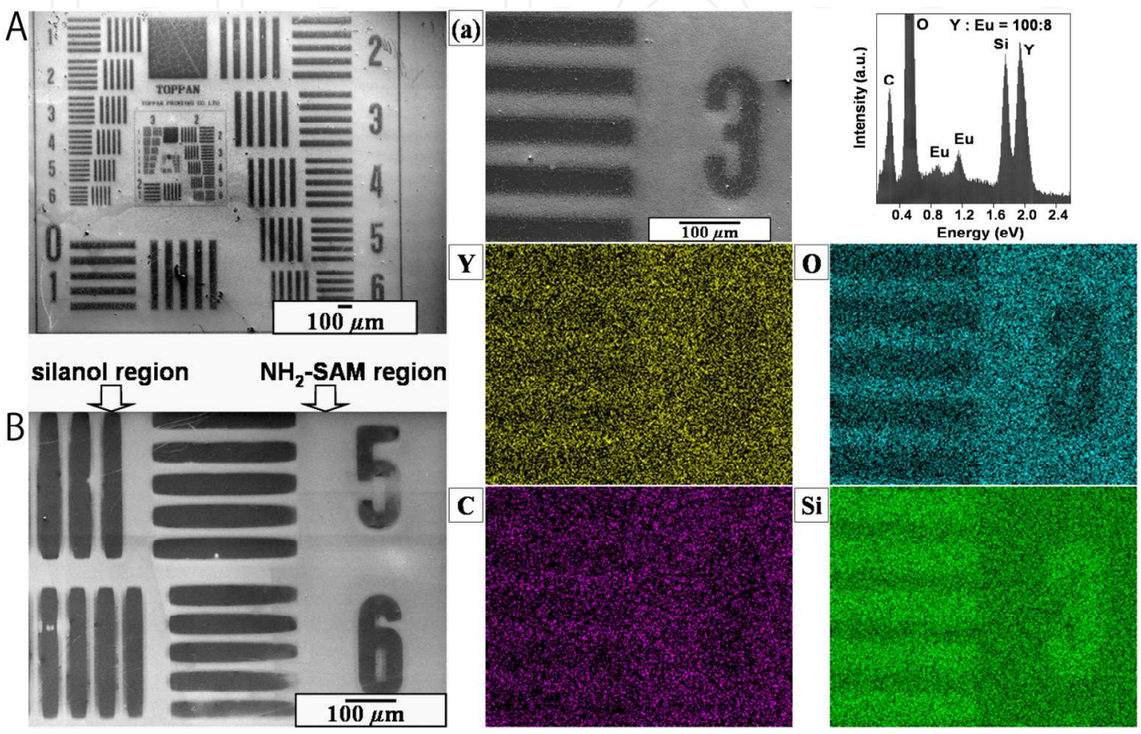

Fig. 11. (A) SEM micrograph of patterned Y_2O_3:Eu thin films and (B) magnified area of (A). (a) SEM micrograph of patterned Y_2O_3:Eu thin films. Characteristic X-ray images of Y, O, C and Si for (a) Y_2O_3:Eu thin films. (Top right) Elemental analysis of Y_2O_3:Eu thin films deposited for 90 min.

Yttrium carbonate films were also deposited on the hydrophobic octadecyl surface of OTS(octadecyltrichlorosilane)-SAM having water contact angle (WCA) of 116 ° and as-purchased silicon wafer having WCA of about 20-50 ° which was kept in a plastic case in air. On the other hand, the films were not deposited on UV irradiated silicon wafer having WCA < 5 °. The super hydrophilic surface of WCA < 5 ° suppressed film deposition, whereas the hydrophobic surface and medium surface of WCA > 20-30 ° accelerated film deposition possibly because of hydrophobic interaction between deposition and substrate surface. This is consistent with a former study[32]. Yttrium carbonate was deposited both on bare single crystal Si wafers, and on Si wafers coated with sulfonate-functionalized organic self-assembled monolayers.

Yttrium, europium, oxygen and carbon were observed from as-deposited thin films on amino regions, while silicon and oxygen were detected from non-covered silanol regions by

EDX (Fig. 11). The molecular ratio of yttrium to europium was determined to be 100 : 8 (Fig. 11). It was close to that of $Y(NO_3)_3 \cdot 6H_2O$ to $Eu(NO_3)_3 \cdot 6H_2O$, i.e., 100 : 10, in the solution because the chemistry of $Eu(NO_3)_3$ is similar to that of $Y(NO_3)_3$ to incorporate europium in the precipitation. The content of europium was in the range we had expected. Y_2O_3:Eu with atomic ratio Y : Eu = 100 : ~ 8 was reported to have strong photoluminescence[27,28]. Carbon was detected from yttrium carbonate. Silicon and oxygen were detected from silicon wafer covered with a natural oxide layer (amorphous SiO_2).

Amino regions were covered with thin films composed of many large particles (about 100–300 nm in diameter) and very high roughness (RMS 25.6 nm) (Fig. 12A). Silanol regions, on the other hand, showed only nano-sized small particles (about 10–50 nm in diameter) and very low roughness (RMS 1.7 nm). The high site-selectivity of deposition and the big difference in surface morphology and roughness were clearly shown by AFM observation. The thickness of the films was estimated from AFM scans across deposited and undeposited regions of the substrate. It increased with immersion time after 45 min (0 nm at 45 min, 60 nm at 70 min and 100 nm at 90 min (Fig. 12A)). The average growth rate (70 nm/h = 100 / 90 min) was higher than that previously reported (2 nm/h = 35 nm / 15 h)[25]. An amorphous yttrium basic carbonate film was deposited at 80 °C from aqueous solutions of $YNO_3 \bullet 5H_2O$ and urea on Si wafers coated with sulfonate-functionalized organic self-assembled monolayers in previous studies. The thickness was then evaluated by TEM after the treatment with ultrasonication for half an hour in distilled water. The difference of growth rate was caused mainly by the difference of the substrate treatment by ultrasonication. Additionally, the thickness of our film was smaller than the particle size in the solution shown in Fig. 10 (227 nm at 100 min). Heterogeneous nucleation and attachment of initial particles of yttrium carbonate occurred without the attachment of aggregated large particles shown in Fig. 10. The yttrium carbonate was then grown on the substrate to form a film of 100 nm thickness after immersion for 90 min. The particles of about 100 nm in height were removed by ultrasonication for 30 min and the film of several nm in height remained as reported[25].

Yttrium was not detected by XPS from the substrate immersed for 45 min, however, it was clearly observed from that immersed for 90 min. This indicates that the deposition began between 45 and 90 min after immersion. The solution temperature reached 70 °C in ~ 45 min and then the solution began to decompose and release carbonate ions, causing the deposition of basic yttrium carbonate. The deposition mechanism evaluated by XPS is consistent with the change of solution temperature, decomposition temperature of urea and chemical reaction of this system. The binding energy of Y 3d5/2 spectrum from the deposition (158.2 eV) was higher than that of metal yttrium (155.8 eV)[29]. The spectrum shifted to lower binding energy (156.7 eV) after annealing at 800 °C in air for 1 h and is similar to that of Y_2O_3 (157.0 eV)[30]. The binding energies of Y 3d5/2 spectra in as-deposited films and annealed films were higher than that of metal yttrium possibly due to the chemical bonds formed between yttrium ions and oxygen ions. The chemical shift of Y 3d5/2 binding energy by annealing is consistent with crystallization of as-deposited films to crystalline Y_2O_3. C 1s spectra were detected at 289.7 eV and 284.6 eV from as-deposited films. The C 1s spectrum at 289.7 eV then disappeared by the annealing. C 1s at 284.6 eV was assigned to surface contamination and C 1s at 289.7 eV was detected from as-deposited

yttrium carbonate. The disappearance of C 1s at 289.7 eV is consistent with the phase transition from yttrium carbonate to Y_2O_3.

As-deposited film was shown to be an amorphous phase (Fig. 12B-a) by XRD measurement. The film showed no diffraction peak after annealing at 400 °C for 1 h, however, it showed 222, 400 and 440 diffraction peaks of crystalline cubic Y_2O_3[31] without any additional phase after annealing at 600 °C for 1 h and the intensities of diffraction peaks increased further by annealing at 800 °C for 1 h (Fig. 12B-b). The film was shown to be a polycrystalline Y_2O_3 film constructed from randomly deposited Y_2O_3 particles without crystal-axis orientation. The crystal structure model and diffraction pattern of Y_2O_3 were calculated from the crystal structure data of ICSD #23811 as shown in Fig. 12B. The crystallization by annealing confirmed from XRD measurement is consistent with XPS evaluation.

We attempted to remove Y_2O_3 films from the silicon substrate by debonding with scotch tape or by ultrasonication for 5 min in water. However, the films maintained their bonds with the substrate, indicating that strong adhesion had formed between films and substrate.

The thin film annealed at 800 °C for 1 h, i.e., crystalline Y_2O_3:Eu thin film, was shown to be excited by 230–250 nm (center: 243 nm) and emit red light photoluminescence centered at 611 nm in the fluorescence excitation spectrum (Fig. 12C-a). Neither the as-deposited film nor the film annealed at 400 °C for 1 h showed photoluminescence, on the other hand, the films annealed at 600 °C or 800 °C for 1 h emitted light centered at 617 nm by 250 nm in fluorescence emission spectra (Fig. 12C-b). The fluorescence intensity of the film annealed at 800 °C was stronger than that of the film annealed at 600 °C. Fluorescence intensity increased by the phase transformation from amorphous yttrium carbonate to yttrium oxide and crystal growth by the heat treatments, and is consistent with the crystallization observed by XRD[32]. The spectra are described by the well-known $^5D_0$–^7F_J line emissions (J = 0, 1, 2, …) of the Eu^{3+} ion with the strongest emission for J = 2 at 612 nm. The thin film annealed at 800 °C produced visible red light photoluminescence by excitation from Nd: YAG laser (266 nm) (Fig. 12C, inset). The white square shows the edges of the Y_2O_3:Eu thin film and the red color shows visible red emission from the irradiated area on the substrate.

In summary, we have proposed a novel process for fabricating visible red light emitting Eu-doped Y_2O_3 and its micropattern using a self-assembled monolayer and an aqueous solution system. The patterned APTS-SAM having amino groups regions and silanol groups regions achieved site-selective deposition of yttrium oxide in an aqueous solution. The deposited films were crystallized by annealing at 600 °C or 800 °C for 1 h. Crystalline Y_2O_3:Eu produced visible red light photoluminescence centered at 611 nm by excitation from Nd: YAG laser (266 nm). This study showed the high potential of aqueous solution systems and self-assembled monolayers for the fabrication of functional metal oxide thin films and their micropatterns.

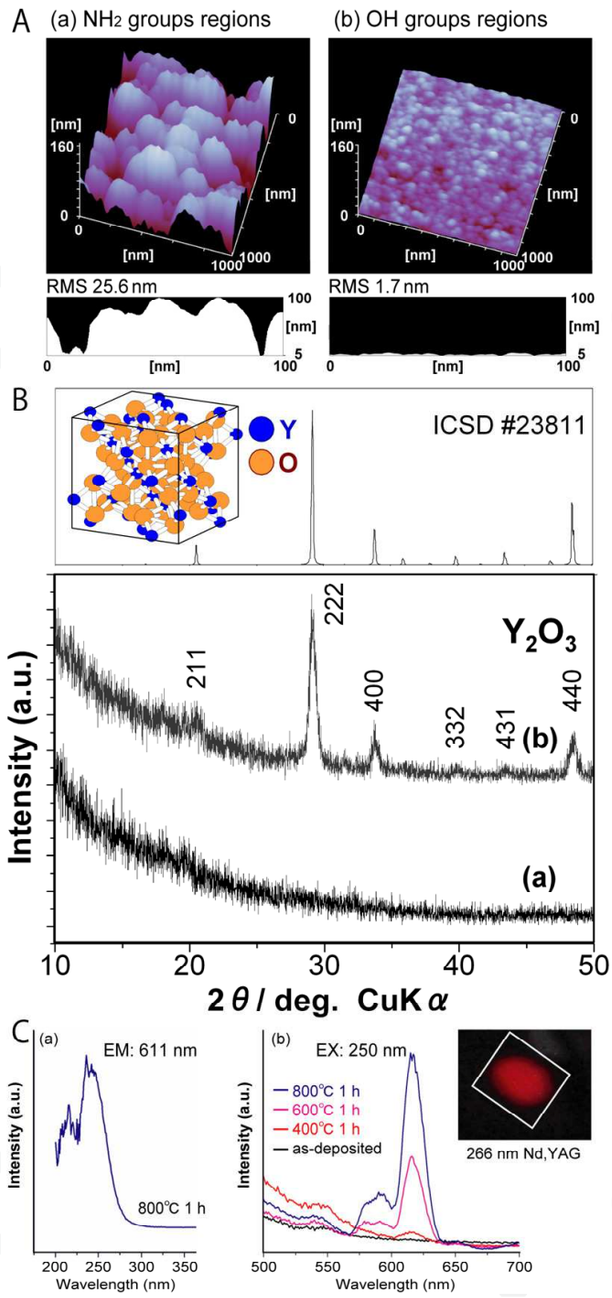

Fig. 12. (A) (a) AFM images and cross-section profile of Y_2O_3:Eu thin films on NH_2 groups regions. (b) AFM images and cross-section profile of Y_2O_3:Eu thin films on OH groups regions. (B) XRD patterns of Y_2O_3:Eu thin films (a) before and (b) after annealing at 800 °C for 1 h. (The upper picture) Crystal structure model and diffraction pattern of cubic Y_2O_3 calculated from crystal structure data of ICSD #23811. (C) (a) Fluorescence excitation spectrum (emission: 611 nm) for Y_2O_3:Eu thin film after annealing at 800 °C for 1 h. (b) Fluorescence emission spectra (excitation: 250 nm) for Y_2O_3:Eu thin films before and after annealing at 400, 600 or 800 °C for 1 h. Inset: Photoluminescence image for Y_2O_3:Eu thin film annealed at 800 °C for 1 h (excitation: 266 nm).

4. Summary

Morphology control, self-assembly and site-selective deposition of metal oxide nanocrystals were reported in this chapter. The novel nano/micro structures of nanocrystals will create the next generation of metal oxide devices. Additionally, they were realized in solutions at ordinary temperature and atmospheric pressure. These environmental-friendly processes will contribute to green innovations.

5. Acknowledgement

The author thanks Prof. Kunihito Koumoto of Nagoya University, Dr. Tatsuki Ohji and Dr. Kazumi Kato of AIST, Dr. Masako Ajimi, Dr. Makoto Bekki and Dr. Shuji Sonezaki of TOTO Ltd. Research Laboratory. Some of works that were reviewed in this chapter were partially supported by METI, Japan, as part of R&D for High Sensitivity Environment Sensor Components.

6. References

(1) Masuda, Y.; Kato, K. *Cryst. Growth Des.* **2008**, *8*, 275-279.
(2) Masuda, Y.; Kato, K. *Cryst. Growth Des.* **2008**, *8*, 3213-3218.
(3) Masuda, Y.; Yamada, T.; Koumoto, K. *Cryst. Growth Des.* **2008**, *8*, 169-171.
(4) Masuda, Y.; Kato, K. *Chem. Mater.* **2008**, *20*, 1057-1063.
(5) Masuda, Y.; Yamagishi, M.; Koumoto, K. *Chem. Mater.* **2007**, *19*, 1002-1008.
(6) Gao, M. D.; Li, M. M.; Yu, W. D. *J. Phys. Chem. B* **2005**, *109*, 1155-1161.
(7) Masuda, Y.; Sugiyama, T.; Seo, W. S.; Koumoto, K. *Chem. Mater.* **2003**, *15*, 2469-2476.
(8) Furlong, D. N.; Parfitt, G. D. *J. Colloid Interface Sci.* **1978**, *65*, 548-554.
(9) Wahi, R. K.; Liu, Y. P.; Falkner, J. C.; Colvin, V. L. *J. Colloid Interface Sci.* **2006**, *302*, 530-536.
(10) Kruk, M.; Jaroniec, M. *Chem. Mater.* **2001**, *13*, 3169-3183.
(11) Ravikovitch, P. I.; Odomhnaill, S. C.; Neimark, A. V.; Schuth, F.; Unger, K. K. *Langmuir* **1995**, *11*, 4765-4772.
(12) Lastoskie, C.; Gubbins, K. E.; Quirke, N. *J. Phys. Chem.* **1993**, *97*, 4786-4796.
(13) Katagiri, K.; Ohno, K.; Masuda, Y.; Koumoto, K. *J. Ceram. Soc. Japan* **2007**, *115*, 831-834.
(14) Mutin, J. C.; Dusausoy, Y.; Protas, J. *J. Solid State Chem.* **1981**, *36*, 356-364.
(15) Potdar, H. S.; Deshpande, S. B.; Date, S. K. *J. Am. Ceram. Soc.* **1996**, *79*, 2795-2797.
(16) Masuda, Y.; Sugiyama, T.; Lin, H.; Seo, W. S.; Koumoto, K. *Thin Solid Films* **2001**, *382*, 153-157.
(17) Dressick, W. J.; Calvert, J. M. *Jpn. J. Appl. Phys.* **1993**, *32*, 5829-5839.
(18) Collins, R. J.; Shin, H.; De Guire, M. R.; Heuer, A. H.; Sukenik, C. N. *Appl. Phys. Lett.* **1996**, *69*, 860-862.
(19) Masuda, Y.; Koumura, T.; Okawa, T.; Koumoto, K. *J. Colloid Interface Sci.* **2003**, *263*, 190-195.
(20) Masuda, Y.; Itoh, M.; Yonezawa, T.; Koumoto, K. *Langmuir* **2002**, *18*, 4155-4159.
(21) Shaw, W. H. R.; Bordeaux, J. J. *J. Am. Chem. Soc.* **1955**, *77*, 4729-4733.
(22) Ryabchikov, D. E.; Ryabukhin, V. A. *Analytical Chemistry of Yttrium and the Lanthanide Elements*; Humphrey Science: Ann Arbor, MI, 1970.

(23) Baes, C. F.; Mesmer, R. E. *The Hydrolysis of Captions*; Wiley: New York, 1976.
(24) Aiken, B.; Hsu, W. P.; Matijevic, E. *J. Am. Ceram. Soc.* **1988**, *71*, 845-853.
(25) Agarwal, M.; DeGuire, M. R.; Heuer, A. H. *Appl. Phys Lett.* **1997**, *71*, 891-893.
(26) Matijevic, E.; Hsu, W. P. *J. Colloid Interface Sci.* **1987**, *118*, 506-523.
(27) Sharma, P. K.; Jilavi, M. H.; Nass, R.; Schmidt, H. *J. Lumin.* **1999**, *82*, 187-193.
(28) Kwaka, M. G.; Parkb, J. H.; Shon, S. H. *Solid State Commun.* **2004**, *130*, 199-201.
(29) Fuggle, J. C.; Martensson, N. *J. Electron Spectrosc. Relat. Phenom.* **1980**, *21*, 275.
(30) Wagner, C. D. *Practical Surface Analysis*; 2 ed.; John Wiley, 1990; Vol. 1.
(31) Paton, M. G.; Maslen, E. N. *Acta Crystallographica* **1967**, *1*, 1948-23.

Figure Captions

Figure 1. SEM micrographs of high *c*-axis oriented stand-alone ZnO self-assembled film. (a1) Air-side surface of ZnO film. (a2) Magnified area of (a1). (b1) Liquid-side surface of ZnO film. (b2) Magnified area of (b2). (c1) Fracture cross section of ZnO film from air side. (c2) Magnified area of (c1). [Reprinted with permission from Ref.[1], Y. Masuda and K. Kato, Cryst. Growth Des. 8, 1, 275, 2008. Copyright @American Chemical Society (2008)]
Figure 2. XRD diffraction pattern of high *c*-axis oriented stand-alone ZnO self-assembled film. (a) TEM micrograph of ZnO nano-sheets. (b) Magnified area of (a). (Insertion) Electron diffraction pattern of ZnO. [Reprinted with permission from Ref.[1], Y. Masuda and K. Kato, Cryst. Growth Des. 8, 1, 275, 2008. Copyright @American Chemical Society (2008)]
Figure 3. SEM micrographs of high *c*-axis oriented stand-alone ZnO self-assembled film annealed at 500°C for 1 h in air. (a1) Fracture edge-on profile of ZnO film from air side. (a2) Cross-section profile of ZnO film from air side. (b1) Fracture edge-on profile of ZnO film from liquid side. (b2) Cross-section profile of ZnO film from liquid side. [Reprinted with permission from Ref.[1], Y. Masuda and K. Kato, Cryst. Growth Des. 8, 1, 275, 2008. Copyright @American Chemical Society (2008)]

Figure 4. XRD diffraction pattern of anatase TiO_2 particles. (a): TEM micrograph of anatase TiO_2 particles. (b): Magnified area of (a) showing morphology of acicular crystals. Insertion in (b): FFT image of (b) anatase TiO_2. (c): Magnified area of (a) showing lattice images of anatase TiO_2. [Reprinted with permission from Ref.[2], Y. Masuda and K. Kato, Crystal Growth & Design, 8, 9, 3213, 2008. Copyright @American Chemical Society (2008)]
Figure 5. (a): N_2 adsorption-desorption isotherm of anatase TiO_2 particles. (b): BET surface area of anatase TiO_2 particles. (c): Pore size distribution calculated from N_2 adsorption data of anatase TiO_2 particles using BJH equation. (d): N_2 adsorption-desorption isotherm and DFT/Monte-Carlo fitting curve of anatase TiO_2 particles. (e): Pore size distribution calculated from N_2 adsorption data of anatase TiO_2 particles using DFT/Monte-Carlo equation. [Reprinted with permission from Ref.[2], Y. Masuda and K. Kato, Crystal Growth & Design, 8, 9, 3213, 2008. Copyright @American Chemical Society (2008)]

Figure 6. (a) Conceptual process for fabricating acicular $BaTiO_3$ particles. Morphology control of $BaC_2O_4 \bullet 0.5H_2O$ particles and phase transition to $BaTiO_3$. (b) SEM micrograph and XRD diffraction pattern of acicular $BaC_2O_4 \bullet 0.5H_2O$ particles precipitated from an aqueous solution at pH = 7. XRD diffraction measurement data (first step), XRD pattern calculated from crystal structure data16 (second step) and XRD pattern of JCPDS No. 20-

134 (third step) are shown for triclinic $BaC_2O_4 \bullet 0.5H_2O$. (c) SEM micrograph and XRD diffraction pattern of acicular $BaTiO_3$ particles after annealing at 750 °C for 5 h and HCl treatment. XRD diffraction measurement data (first step) and XRD pattern of JCPDS No. 05-0626 (second step) are shown for tetragonal $BaTiO_3$. [Reprinted with permission from Ref. [3], Y. Masuda, T. Yamada and K. Koumoto, Cryst. Growth Des. 8, 169, 2008. Copyright @American Chemical Society (2008)]

Figure 7. Conceptual process for liquid phase patterning of anatase TiO_2 films using super-hydrophilic surface. XRD diffraction pattern of anatase TiO_2 film on a glass substrate. [Reprinted with permission from Ref.[4], Y. Masuda and K. Kato, Chem. Mater., 20, 3, 1057, 2008. Copyright @American Chemical Society (2008)]

Figure 8. SEM micrographs of a micropattern of anatase TiO_2 films on SnO_2: F substrates. (Top) Micropattern of anatase TiO_2 films. (a1) Surface of anatase TiO_2 films deposited on super-hydrophilic region. TiO_2 was formed on super-hydrophilic region which was cleaned by UV irradiation before the immersion. (a2) Magnified area of (a1) showing surface morphology of anatase TiO_2 film. (b1) Surface of SnO_2: F substrate without TiO_2 deposition. TiO_2 was not formed on non-cleaned region. (b2) Magnified area of (b1) showing surface morphology of SnO_2: F substrate. [Reprinted with permission from Ref.[4], Y. Masuda and K. Kato, Chem. Mater., 20, 3, 1057, 2008. Copyright @American Chemical Society (2008)]

Figure 9. SEM micrographs of anatase TiO_2 films on SnO_2: F substrates. (a) Fracture cross section of TiO_2 films. (b, c) Magnified area of (a) showing morphology of nano TiO_2 crystals. [Reprinted with permission from Ref.[4], Y. Masuda and K. Kato, Chem. Mater., 20, 3, 1057, 2008. Copyright @American Chemical Society (2008)]

Figure 10. Conceptual process for site-selective deposition of visible-light emitting Y_2O_3:Eu thin films using a self-assembled monolayer. (a) Time variation of particle size distribution. (1-5) Particle size distribution of yttrium carbonate particles at (1) 100 min, (2) 150 min, (3) 180 min, (4) 210 min or (5) 240 min. [Reprinted with permission from Ref.[5], Y. Masuda, M. Yamagishi, K. Koumoto, Chem. Mater., 19, 1002, 2007. Copyright @American Chemical Society (2007)]

Figure 11. (A) SEM micrograph of patterned Y_2O_3:Eu thin films and (B) magnified area of (A). (a) SEM micrograph of patterned Y_2O_3:Eu thin films. Characteristic X-ray images of Y, O, C and Si for (a) Y_2O_3:Eu thin films. (Top right) Elemental analysis of Y_2O_3:Eu thin films deposited for 90 min. [Reprinted with permission from Ref.[5], Y. Masuda, M. Yamagishi, K. Koumoto, Chem. Mater., 19, 1002, 2007. Copyright @American Chemical Society (2007)]

Figure 12. (A) (a) AFM images and cross-section profile of Y_2O_3:Eu thin films on NH_2 groups regions. (b) AFM images and cross-section profile of Y_2O_3:Eu thin films on OH groups regions. (B) XRD patterns of Y_2O_3:Eu thin films (a) before and (b) after annealing at 800 °C for 1 h. (The upper picture) Crystal structure model and diffraction pattern of cubic Y_2O_3 calculated from crystal structure data of ICSD #23811. (C) (a) Fluorescence excitation spectrum (emission: 611 nm) for Y_2O_3:Eu thin film after annealing at 800 °C for 1 h. (b) Fluorescence emission spectra (excitation: 250 nm) for Y_2O_3:Eu thin films before and after annealing at 400, 600 or 800 °C for 1 h. Inset: Photoluminescence image for Y_2O_3:Eu thin film annealed at 800 °C for 1 h (excitation: 266 nm). [Reprinted with permission from Ref.[5], Y. Masuda, M. Yamagishi, K. Koumoto, Chem. Mater., 19, 1002, 2007. Copyright @American Chemical Society (2007)]

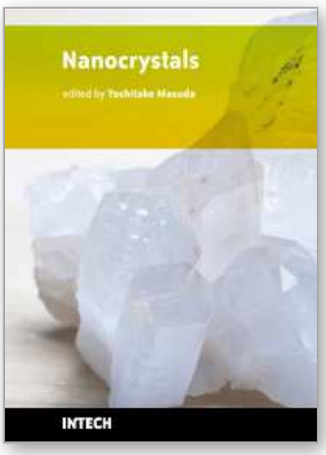

Nanocrystals

Edited by Yoshitake Masuda

ISBN 978-953-307-126-8
Hard cover, 326 pages
Publisher Sciyo
Published online 06, October, 2010
Published in print edition October, 2010

This book contains a number of latest research developments on nanocrystals. It is a promising new research area that has received a lot of attention in recent years. Here you will find interesting reports on cutting-edge science and technology related to synthesis, morphology control, self-assembly and application of nanocrystals. I hope that the book will lead to systematization of nanocrystal science, creation of new nanocrystal research field and further promotion of nanocrystal technology for the bright future of our children.

How to reference

In order to correctly reference this scholarly work, feel free to copy and paste the following:

Yoshitake Masuda (2010). Morphology Control, Self-Assembly and Site-Selective Deposition of Nanocrystals, Nanocrystals, Yoshitake Masuda (Ed.), ISBN: 978-953-307-126-8, InTech, Available from: http://www.intechopen.com/books/nanocrystals/morphology-control-self-assembly-and-site-selective-deposition-of-nanocrystals

INTECH
open science | open minds

InTech Europe
University Campus STeP Ri
Slavka Krautzeka 83/A
51000 Rijeka, Croatia
Phone: +385 (51) 770 447
Fax: +385 (51) 686 166
www.intechopen.com

InTech China
Unit 405, Office Block, Hotel Equatorial Shanghai
No.65, Yan An Road (West), Shanghai, 200040, China
中国上海市延安西路65号上海国际贵都大饭店办公楼405单元
Phone: +86-21-62489820
Fax: +86-21-62489821

IntechOpen